A Linearized Cascade-Free Continuous Control Set Model Predictive Control Algorithm for Modular Multilevel Matrix Converters

Matias Uriarte, *Graduate Student Member, IEEE*, Roberto Cardenas-Dobson, *Senior Member, IEEE*, Yeiner Arias-Esquivel, *Member, IEEE*, Luca Tarisciotti, *Senior Member, IEEE*, Matías Díaz, *Senior Member, IEEE*, and Oriol Gomis-Bellmunt, *Fellow, IEEE*

***Abstract*—Modular Multilevel Matrix Converters (M3C) provide an efficient solution for high-power ac-to-ac conversion, offering high modularity, superior power quality, and reduced power filtering requirements. However, controlling their Circulating Currents (CCs) and Cluster Capacitor Voltages (CCVs) remains a significant challenge due to the strong coupling between system variables. To address these issues, this article presents a novel cascade-free model predictive control strategy that introduces a linearized M3C model, incorporating the Common-Mode Voltage (CMV) as an additional control input. Unlike conventional control structures relying on multiple nested loops or iterative procedures, the proposed approach computes all control actions in a single stage by solving a constrained optimization problem. Simulation and experimental results demonstrate that the proposed methodology effectively reduces CCV fluctuations and lowers the magnitude of CCs (peaks and effective values), even under constrained operating conditions. These results confirm that including the CMV as a control input provides additional degrees of freedom, making it a compelling alternative for high-performance M3C applications.**

***Index Terms*—Cascade-free control, circulating currents, common-mode voltage (CMV), model predictive control (MPC), modular multilevel matrix converter (M3C).**

Received 23 March 2025; revised 15 June 2025 and 19 August 2025; accepted 23 September 2025. Date of publication 29 September 2025; date of current version 13 November 2025. This work was supported in part by ANID Beca Doctorado Nacional under Grant 21230608, in part by ANID through Fondecyt projects under Grant 1221392, Grant 1240046, and Grant 1230596, in part by ANID Anillo under Grant ATE230035, in part by ANID Basal project under Grant AFB240002, in part by ANID Fondequip under Grant EQM200234, and in part by the Costa Rica Institute of Technology under VIE Project under Grant 5402-1320-0004. Recommended for publication by Associate Editor Q. Wei. *(Corresponding author: Roberto Cardenas-Dobson.)*

Matias Uriarte is with the University of Santiago of Chile, Santiago 9170124, Chile, also with the University of Chile, Santiago 8370451, Chile, and also with the Technical University of Catalonia, 08028 Barcelona, Spain (e-mail: matias.uriarte@usach.cl).

Roberto Cardenas-Dobson is with the University of Chile, Santiago 8370451, Chile (e-mail: jesus.cardenas@uchile.cl).

Yeiner Arias-Esquivel is with the Institute of Technology, Cartago 30101, Costa Rica (e-mail: yarias@tec.ac.cr).

Luca Tarisciotti is with the Department of Engineering, Universidad Andres Bello, Santiago 8370035, Chile (e-mail: luca.tarisciotti@unab.cl).

Matías Díaz is with the University of Santiago of Chile, Santiago 9170124, Chile (e-mail: matias.diazd@usach.cl).

Oriol Gomis-Bellmunt is with the Technical University of Catalonia, 08028 Barcelona, Spain (e-mail: oriol.gomis@upc.edu).

Color versions of one or more figures in this article are available at https://doi.org/10.1109/TPEL.2025.3615848.

Digital Object Identifier 10.1109/TPEL.2025.3615848

Nomenclature

M3C	Modular Multilevel Matrix Converter.
CC	Circulating Current.
CCV	Cluster Capacitor Voltage.
MPC	Model Predictive Control.
CMV	Common-Mode Voltage.
WECS	Wind Energy Conversion System.
MIMO	Multiple-Input Multiple-Output.
SISO	Single-Input Single-Output.
CCS-MPC	Continuous Control Set MPC.
FCS-MPC	Finite Control Set MPC.
SS-CCV	Single-Stage CCV.
PWM	Pulse-Width Modulation.
LS-PWM	Level-Shifted PWM.
IPD-PWM	In-Phase carrier Disposition PWM.
SM	Semiconductor Module.

I. Introduction

THE M3C has emerged as a promising solution for high-power ac-to-ac direct conversion applications. Its versatility makes it well-suited for a variety of applications, including electrical machine drives [1], [2], [3], [4], WECS [5], low-frequency power transmission systems [6], [7], [8], and flywheel energy storage systems [9]. According to [10], the M3C is potentially poised to replace cyclo converters shortly.

M3Cs are characterized by their high performance, modularity, high power quality, and elimination of the need for bulky filters and transformers, with the main challenge being the converter control [11], [12], [13]. The M3C consists of nine clusters, each composed of a series connection of H-Bridge power submodules, as shown in Fig. 1(a). These submodules are connected to flying capacitors, which are not linked to external voltage sources, making it crucial to regulate their voltage for the correct operation of the converter. The regulation of the capacitor voltages becomes particularly complex when the frequencies of the ac systems connected to the M3C ports are similar or equal, as this can lead to dangerous voltage oscillations in the capacitors. For this reason, controlling the CCVs, i.e. the sum of the voltages across the capacitors within a cluster, is of utmost importance, because these CCVs must be regulated to a predefined value to ensure stable operation [3], [11]. To achieve this, the M3C can

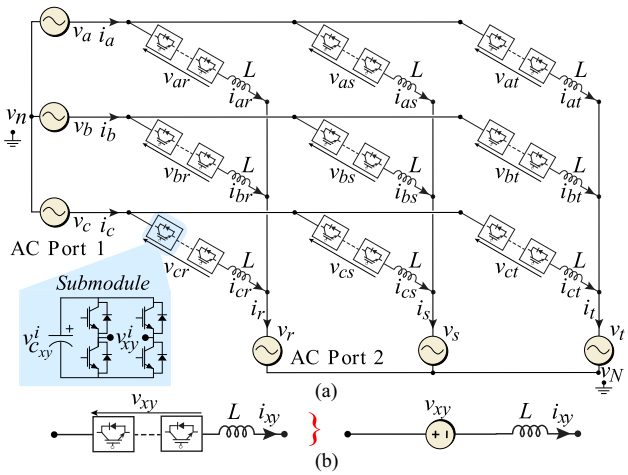

Fig. 1. M3C Circuit configuration. (a) Full converter topology and (b) cluster equivalent circuit, i.e. a voltage source and an inductance in series connection.

employ up to five control inputs specifically designed to regulate capacitor voltage oscillations. However, the system dynamics are highly coupled, which poses complex control challenges. For CCV regulation, the M3C typically utilises four CCs and the CMV, the latter often applied as a predefined signal [2], [6].

Even when the M3C is a MIMO system, with five control inputs utilized to control the capacitor voltages and mitigate oscillations, strategies based on SISO control loops are commonly proposed in the literature. These strategies typically rely on electrical coordinate transformations such as the double $\alpha\beta 0$ [14] or the double $\alpha\beta 0\Sigma\Delta$ transform [5], [15], [16], which use the CCs to regulate the CCVs. However, they cannot eliminate the coupling between the control loops of CCs of different frequencies and sequences. For example, the strategies reported in [1] and [17] use several PI controllers, assuming for their design that each SISO control loop is fully decoupled from the others, which is a gross oversimplification [18]. Another problem of implementing multiple SISO control loops is the difficulty of handling constraints. Constraining the addition of several CC components in a cluster, using conventional anti-windup schemes, is suboptimal, as discussed in [19].

For these reasons, MPC strategies are often proposed as suitable alternatives for MIMO design in highly coupled multivariable systems, such as M3Cs. MPC controllers can regulate multiple targets within a single cost function, they have a good dynamic response, and constraint handling is simple to achieve. CCS-MPC strategies have recently been proposed for regulating modular multilevel converters [18], [19], [20], and one of the advantages of CCS-MPC implementation is a relatively low computational burden because it utilises an external modulator. Therefore, the processing burden no longer depends on the number of switching states, as is the case with most MPC solutions using FCS-MPC algorithms [21], [22]. The first works discussing CCS-MPC algorithms for M3C applications were presented in [19], [23], and[24]; however, in these papers, nested or cascaded control loops are used in the proposed CCS-MPC algorithms. Cascade-free algorithms have some advantages over nested MPC loops because of: 1) if nested CCS-MPC algorithms are used, e.g., an external MPC to regulate the CCVs and an internal one to control the CCs, then the external controller is usually designed with a smaller bandwidth to reduce the cross-coupling between the nested controllers. This methodology can produce a relatively low dynamic response in the CCVs, particularly when the switching frequency is low and, consequently, the bandwidths of the circulating-current control loops are not high [25]; 2) with nested CCS-MPC algorithms, there are two cost functions which are separately solved and a global optimum is not necessarily reached [18]; 3) it is challenging to implement constraints which simultaneously involve variables of the external and internal loops because their respective cost functions are sequentially solved and a causality dilemma could be produced. A possible disadvantage of cascade-free algorithms is that a single global problem involving more state variables, more control actions, and a more complex optimal problem must be solved in each sampling period. However, for an M3C topology regulated using a modern control platform, the additional complexity is almost negligible.

In addition to the cascade control loops, in most of the works discussing CCS-MPC algorithms for modular multilevel converters, a mixture of SISO and MIMO-designed control loops is implemented. For instance, in [19], a CCS-MPC methodology was proposed to control the M3C CCs, considering constraints. However, the control of the CCVs is performed using multiple SISO-designed controllers. An approach based on dead-beat control was proposed in [26] for controlling the CCs and ac ports currents of an M3C. The cost function only considers the tracking error in the circulating currents, and multiple SISO-designed controllers generate the references for the CCs. A saturation algorithm, not considered in the cost function, is implemented to avoid overmodulation in [26]. In [23], a CCS-MPC algorithm was proposed to regulate the oscillations of the CCVs; nevertheless, in this article, the CCs obtained from the external CCS-MPC algorithm are regulated using SISO-designed PI controllers. In addition, no constraints are considered in [23]. The work of [24] proposed a three-nested control loop structure to regulate the M3C. In this case, the common-mode voltage is considered an additional control action and regulated by an MPC in the outermost control loop. The next control layer is a CCS-MPC algorithm regulating the CCVs. Finally, the innermost control loop is based on SISO-designed proportional controllers regulating the CCs. Recently, a similar approach has been proposed in [27], where an iterative optimization process is added between the CMV and the CCs by separating the nonlinear terms, produced by the multiplication of the CMV with the CCs, into two linear problems. Similarly, in [28], an iterative optimization process to determine the CMV and the CCs is used, and an additional optimization problem is added to regulate the converter currents. However, finding the optimal control action could result in an increased computational burden caused by the iterative process. Moreover, cascade-free algorithms were not used in [27], [24], and [28]. This work addresses some of the problems reported in the literature regarding the implementation of a cascade-free CCS-MPC algorithm considering the CMV as a control input. The contributions of this work are summarized as follows.

1) The CCS-MPC algorithm proposed in this work to regulate the M3C utilizes a linearized model, enabling the inclusion of the CMV as an additional control input. With the proposed methodology, the input vector $\boldsymbol{u}$ in the state-space formulation contains five elements: Four voltages driving the circulating currents and the CMV. Consequently, the CMV can be used to reduce the effective and peak value of the CCs. Furthermore, the fast dynamics of the CMV can be used to compensate for high-dynamic perturbations.
2) This article presents a single-stage, or cascade-free, CCS-MPC control strategy, where a single cost function is utilized to regulate the CCVs, CMV, and CCs optimally. Unlike [27], no iterative procedure is required; neither the three nested control loops of [24] nor the SISO-designed controllers in the innermost control loops of [19], [23], [24], and [27] are necessary. The algorithm proposed in this work is a full cascade-free CCS-MPC, where every control input is calculated, in a single-stage implementation, at each sampling step by solving a constrained cost function.

The rest of this article is organized as follows. In Section II, the state-space modeling of the M3C is briefly discussed, and in Section III, the proposed CCS-MPC is analyzed. The dynamic and steady state performance of the CCS-MPC algorithm discussed in this work is compared with two other control methodologies in Section IV. Section V discusses the experimental results. Finally, Section VI concludes this article and an appraisal of the proposed system is also presented.

II. Modeling of the M3C

The M3C model used in this publication is based on the works of [7], [14], [16]; for completeness, the modeling is briefly reviewed below in Section II-A.

A. Using the Double $\alpha\beta0\Sigma\Delta$ Transform to Obtain the Power Model of the M3C

Applying Kirchhoff's voltage law at the circuit of Fig. 1(a) and using the cluster equivalent circuit of Fig. 1(b), the voltage-current model can be obtained as follows:

$$v_x = L\frac{d}{dt}i_{xy} + v_{xy} + v_y + v_{nN} \tag{1}$$

where $x \in \{a,b,c\}$, $y \in \{r,s,t\}$, and v_{nN} represents the CMV. To partially decouple the dynamics of the M3C, the double $\alpha\beta0$ frame is used. If the model of M3C in rst-abc coordinates is denoted as $\mathbf{X}_{abc}^{rst}$, then the model in the double $\alpha\beta0$ frame is obtained by ${\mathbf{T}_{\alpha\beta0}}^T\mathbf{X}_{abc}^{rst}\mathbf{T}_{\alpha\beta0}$ where $\mathbf{T}_{\alpha\beta0}$ represents the power-invariant Clarke transformation [3].

By applying the double $\alpha\beta0$ transformation to (1), the following model is derived and presented as follows:

$$\sqrt{3}\begin{bmatrix}0&0&0\\0&0&0\\v_{1\alpha}&v_{1\beta}&0\end{bmatrix} = L\frac{d}{dt}\begin{bmatrix}i_{\alpha\alpha}&i_{\beta\alpha}&i_{0\alpha}\\i_{\alpha\beta}&i_{\beta\beta}&i_{0\beta}\\i_{\alpha0}&i_{\beta0}&0\end{bmatrix} + \begin{bmatrix}v_{\alpha\alpha}&v_{\beta\alpha}&v_{0\alpha}\\v_{\alpha\beta}&v_{\beta\beta}&v_{0\beta}\\v_{\alpha0}&v_{\beta0}&v_{00}\end{bmatrix} + \sqrt{3}\begin{bmatrix}0&0&v_{2\alpha}\\0&0&v_{2\beta}\\0&0&0\end{bmatrix} + \begin{bmatrix}0&0&0\\0&0&0\\0&0&3v_{nN}\end{bmatrix}. \tag{2}$$

Here, the subscripts 1 and 2 denote the currents and voltages at the ac ports 1 and 2, respectively, and the voltage v_{00} is proportional to the CMV. To further decouple frequency components and simplify the control of the M3C, an additional transformation is applied. The $\Sigma\Delta$ transform is defined as follows:

$$\underbrace{\begin{bmatrix}X_{1\alpha}^{\Sigma\Delta}\\X_{1\beta}^{\Sigma\Delta}\\X_{2\alpha}^{\Sigma\Delta}\\X_{2\beta}^{\Sigma\Delta}\end{bmatrix}}_{X_{\Sigma\Delta}} = \underbrace{\frac{1}{2}\begin{bmatrix}1&0&0&1\\0&1&-1&0\\1&0&0&-1\\0&1&1&0\end{bmatrix}}_{\mathbf{T\Sigma\Delta}}\begin{bmatrix}X_{\alpha\alpha}\\X_{\alpha\beta}\\X_{\beta\alpha}\\X_{\beta\beta}\end{bmatrix}. \tag{3}$$

By applying (3) to (2), the following decoupled model is obtained:

$$\sqrt{3}\begin{bmatrix}0&0&0\\0&0&0\\v_{1\alpha}&v_{1\beta}&0\end{bmatrix} = L\frac{d}{dt}\begin{bmatrix}i_{1\alpha}^{\Sigma\Delta}&i_{2\alpha}^{\Sigma\Delta}&i_{0\alpha}\\i_{1\beta}^{\Sigma\Delta}&i_{2\beta}^{\Sigma\Delta}&i_{0\beta}\\i_{\alpha0}&i_{\beta0}&0\end{bmatrix} + \begin{bmatrix}v_{1\alpha}^{\Sigma\Delta}&v_{2\alpha}^{\Sigma\Delta}&v_{0\alpha}\\v_{1\beta}^{\Sigma\Delta}&v_{2\beta}^{\Sigma\Delta}&v_{0\beta}\\v_{\alpha0}&v_{\beta0}&v_{00}\end{bmatrix} + \sqrt{3}\begin{bmatrix}0&0&v_{2\alpha}\\0&0&v_{2\beta}\\0&0&0\end{bmatrix} + \begin{bmatrix}0&0&0\\0&0&0\\0&0&3v_{nN}\end{bmatrix}. \tag{4}$$

In this model, the voltages $v_{1\alpha}^{\Sigma\Delta}$, $v_{1\beta}^{\Sigma\Delta}$, $v_{2\alpha}^{\Sigma\Delta}$, and $v_{2\beta}^{\Sigma\Delta}$ are part of the single-stage control input in the state-space formulation proposed in this work. The currents $i_{1\alpha}^{\Sigma\Delta}$, $i_{1\beta}^{\Sigma\Delta}$, $i_{2\alpha}^{\Sigma\Delta}$, and $i_{2\beta}^{\Sigma\Delta}$ represent the internal CCs of the M3C. The CCs are defined as four-state variables, and a state-space model can represent their dynamics. The state equations of the CCs can be derived from (4) as

$$\dot{\boldsymbol{x}}^i = \boldsymbol{A}^i\boldsymbol{x}^i + \boldsymbol{B}^i\boldsymbol{u}^i \tag{5}$$

where $\boldsymbol{A}^i$ is a 4×4 zero matrix, and matrices $\boldsymbol{B}^i$ (4×4 matrix), $\boldsymbol{x}^i$ (4×1) and $\boldsymbol{u}$ (4×1) are defined as

$$\boldsymbol{B}^i = -\frac{1}{L}\boldsymbol{I} \tag{6a}$$

$$\boldsymbol{x}^i = \begin{bmatrix}i_{1\alpha}^{\Sigma\Delta} & i_{1\beta}^{\Sigma\Delta} & i_{2\alpha}^{\Sigma\Delta} & i_{2\beta}^{\Sigma\Delta}\end{bmatrix}^T \tag{6b}$$

$$\boldsymbol{u}^i = \begin{bmatrix}v_{1\alpha}^{\Sigma\Delta} & v_{1\beta}^{\Sigma\Delta} & v_{2\alpha}^{\Sigma\Delta} & v_{2\beta}^{\Sigma\Delta}\end{bmatrix}^T \tag{6c}$$

where $\boldsymbol{I}$ is a 4×4 identity matrix, and L is the cluster inductance as shown in Fig. 1(b).

Considering any of the clusters shown in Fig. 1(a), its CCV is defined as

$$v_{c_{xy}} = \sum_{\mathrm{i}=1}^{n} v_{c_{xy}}^{\mathrm{i}} \tag{7}$$

where n is the number of submodules in the cluster xy. Assuming that the local balance works correctly and that the voltage of all capacitors in the same cluster have the same

value, i.e., $v_{c_{xy}}^1 = v_{c_{xy}}^2 = \ldots = v_{c_{xy}}^n = v_{c_{xy}}$, the relationships between these capacitor voltages and power elements are given as [14]

$$v_{c_{xy}} \approx n\bar{v}_c + \frac{1}{nC\bar{v}_c}\int P_{xy}dt. \tag{8}$$

Applying double $\alpha\beta 0$ and $\Sigma\Delta$ transformation to (8) yields

$$\begin{bmatrix} v_{c_{1\alpha}^{\Sigma\Delta}} & v_{c_{2\alpha}^{\Sigma\Delta}} & v_{c_{0\alpha}^{\Sigma\Delta}} \\ v_{c_{1\beta}^{\Sigma\Delta}} & v_{c_{2\beta}^{\Sigma\Delta}} & v_{c_{0\beta}^{\Sigma\Delta}} \\ v_{c_{\alpha 0}^{\Sigma\Delta}} & v_{c_{\beta 0}^{\Sigma\Delta}} & v_{c_{00}^{\Sigma\Delta}} \end{bmatrix} \approx \begin{bmatrix} 0 & 0 & 0 \\ 0 & 0 & 0 \\ 0 & 0 & 3n\bar{v}_c \end{bmatrix} + \frac{1}{nC\bar{v}_c}\int \begin{bmatrix} P_{1\alpha}^{\Sigma\Delta} & P_{2\alpha}^{\Sigma\Delta} & P_{0\alpha}^{\Sigma\Delta} \\ P_{1\beta}^{\Sigma\Delta} & P_{2\beta}^{\Sigma\Delta} & P_{0\beta}^{\Sigma\Delta} \\ P_{\alpha 0}^{\Sigma\Delta} & P_{\beta 0}^{\Sigma\Delta} & P_{00}^{\Sigma\Delta} \end{bmatrix} dt. \tag{9}$$

The term $v_{c_{00}^{\Sigma\Delta}}$ is related to the total active power flowing into or from the M3C, denoted as $P_{00}^{\Sigma\Delta}$. This term can be regulated to set the average total value of the CCVs, which can be calculated as follows:

$$P_{00}^{\Sigma\Delta} \approx \frac{1}{3}\underbrace{(i_{1\alpha}v_{1\alpha} + i_{1\beta}v_{1\beta})}_{\textbf{AC Port 1 Power}} - \frac{1}{3}\underbrace{(i_{2\alpha}v_{2\alpha} + i_{2\beta}v_{2\beta})}_{\textbf{AC Port 2 Power}}. \tag{10}$$

The remaining eight transformed voltage terms from (9) represent CCV imbalances and have to be driven to ≈ 0 when the M3C AC voltages are balanced and all the CCVs are $\approx \bar{v}_c$. The eight power terms on the right-hand side of (9) can also be expressed as a function of the transformed currents and voltages of the converter as follows:

$$P_{1\alpha}^{\Sigma\Delta} \approx \frac{1}{6}(i_{2\alpha}v_{1\alpha} - i_{1\alpha}v_{2\alpha} + i_{2\beta}v_{1\beta} - i_{1\beta}v_{2\beta}) + \frac{\sqrt{6}}{6}(i_{2\alpha}^{\Sigma\Delta}v_{1\alpha} - i_{2\beta}^{\Sigma\Delta}v_{1\beta} + i_{2\beta}^{\Sigma\Delta}v_{2\beta} - i_{2\alpha}^{\Sigma\Delta}v_{2\alpha}) + \frac{1}{3}i_{1\alpha}^{\Sigma\Delta}v_{00} \tag{11a}$$

$$P_{1\beta}^{\Sigma\Delta} \approx \frac{1}{6}(i_{2\beta}v_{1\alpha} - i_{1\alpha}v_{2\beta} - i_{2\alpha}v_{1\beta} + i_{1\beta}v_{2\alpha}) + \frac{\sqrt{6}}{6}(i_{2\beta}^{\Sigma\Delta}v_{1\alpha} + i_{2\alpha}^{\Sigma\Delta}v_{1\beta} + i_{2\beta}^{\Sigma\Delta}v_{2\alpha} + i_{2\alpha}^{\Sigma\Delta}v_{2\beta}) + \frac{1}{3}i_{1\beta}^{\Sigma\Delta}v_{00} \tag{11b}$$

$$P_{0\alpha}^{\Sigma\Delta} \approx \frac{\sqrt{2}}{6}(i_{2\beta}v_{2\beta} - i_{2\alpha}v_{2\alpha}) + \frac{\sqrt{3}}{3}((i_{1\alpha}^{\Sigma\Delta} + i_{2\alpha}^{\Sigma\Delta})v_{1\alpha} + (-i_{1\beta}^{\Sigma\Delta} + i_{2\beta}^{\Sigma\Delta})v_{1\beta}) + \frac{\sqrt{3}}{9}i_{2\alpha}v_{00} \tag{11c}$$

$$P_{2\alpha}^{\Sigma\Delta} \approx \frac{1}{6}(i_{2\alpha}v_{1\alpha} - i_{1\alpha}v_{2\alpha} - i_{2\beta}v_{1\beta} + i_{1\beta}v_{2\beta}) + \frac{\sqrt{6}}{6}(i_{1\alpha}^{\Sigma\Delta}v_{1\alpha} + i_{1\beta}^{\Sigma\Delta}v_{1\beta} + i_{1\beta}^{\Sigma\Delta}v_{2\beta} - i_{1\alpha}^{\Sigma\Delta}v_{2\alpha}) + \frac{1}{3}i_{2\alpha}^{\Sigma\Delta}v_{00} \tag{11d}$$

$$P_{2\beta}^{\Sigma\Delta} \approx \frac{1}{6}(i_{2\beta}v_{1\alpha} - i_{1\alpha}v_{2\beta} + i_{2\alpha}v_{1\beta} - i_{1\beta}v_{2\alpha}) + \frac{\sqrt{6}}{6}(i_{1\beta}^{\Sigma\Delta}v_{1\alpha} - i_{1\alpha}^{\Sigma\Delta}v_{1\beta} + i_{1\beta}^{\Sigma\Delta}v_{2\alpha} + i_{1\alpha}^{\Sigma\Delta}v_{2\beta}) + \frac{1}{3}i_{2\beta}^{\Sigma\Delta}v_{00} \tag{11e}$$

$$P_{0\beta}^{\Sigma\Delta} \approx \frac{\sqrt{2}}{6}(i_{2\alpha}v_{2\beta} + i_{2\beta}v_{2\alpha}) + \frac{\sqrt{3}}{3}((i_{1\beta}^{\Sigma\Delta} + i_{2\beta}^{\Sigma\Delta})v_{1\alpha} + (i_{1\alpha}^{\Sigma\Delta} - i_{2\alpha}^{\Sigma\Delta})v_{1\beta}) + \frac{\sqrt{3}}{9}i_{2\beta}v_{00} \tag{11f}$$

$$P_{\alpha 0}^{\Sigma\Delta} \approx -\frac{\sqrt{2}}{6}(i_{1\alpha}v_{1\alpha} + i_{1\beta}v_{1\beta}) - \frac{\sqrt{3}}{3}((i_{1\alpha}^{\Sigma\Delta} + i_{2\alpha}^{\Sigma\Delta})v_{2\alpha} + (i_{1\beta}^{\Sigma\Delta} + i_{2\beta}^{\Sigma\Delta})v_{2\beta}) + \frac{\sqrt{3}}{9}i_{1\alpha}v_{00} \tag{11g}$$

$$P_{\beta 0}^{\Sigma\Delta} \approx -\frac{\sqrt{2}}{6}(i_{1\alpha}v_{1\beta} + i_{1\beta}v_{1\alpha}) - \frac{\sqrt{3}}{3}((-i_{1\beta}^{\Sigma\Delta} + i_{2\beta}^{\Sigma\Delta})v_{2\alpha} + (i_{1\alpha}^{\Sigma\Delta} - i_{2\alpha}^{\Sigma\Delta})v_{2\beta}) + \frac{\sqrt{3}}{9}i_{1\beta}v_{00}. \tag{11h}$$

Using (9), (11) and after some mathematical manipulations, it is concluded (see [15]) that the capacitor voltages $v_{c_{1\alpha}^{\Sigma\Delta}}$ and $v_{c_{1\beta}^{\Sigma\Delta}}$ are prone to large voltage fluctuations when $f_1 \approx f_2$. The terms $v_{c_{2\alpha}^{\Sigma\Delta}}$ and $v_{c_{1\beta}^{\Sigma\Delta}}$ may have large voltage fluctuations when $f_1 \approx -f_2$. Finally, relatively large voltage fluctuations may be produced in $v_{c_{\alpha 0}^{\Sigma\Delta}}$ and $v_{c_{\beta 0}^{\Sigma\Delta}}$ when $f_1 \approx 0$ and in $v_{c_{0\alpha}^{\Sigma\Delta}}$ and $v_{c_{0\beta}^{\Sigma\Delta}}$ when $f_2 \approx 0$.

The control strategy proposed in this work aims to control the CCVs over a wide operating frequency range, including the previously mentioned critical points. The proposed control strategy is based on regulating the CCVs using five degrees of freedom, the four voltages of (6) and v_{00}.

B. Linearized Model to Add the CMV as a Control Input

If the CMV is not considered as a manipulable control input, the control vector $\boldsymbol{u}$ is equal to $[v_{1\alpha}^{\Sigma\Delta}, v_{1\beta}^{\Sigma\Delta}, v_{2\alpha}^{\Sigma\Delta}, v_{2\beta}^{\Sigma\Delta}]^T$; in this case the CMV is considered as a predefined waveform in the control system, e.g., typically a third harmonic of the grid voltage. However, as discussed in the contributions, some advantages exist in allowing the CCS-MPC to calculate the optimal CMV to be applied to the M3C, reducing the CCs magnitude and improving the dynamic response. Nevertheless, to add v_{00} to $\boldsymbol{u}$, a linearized model is required, and this is discussed below.

The capacitor voltages, e.g., $v_{c_{1\alpha}^{\Sigma\Delta}}$ and $v_{c_{1\beta}^{\Sigma\Delta}}$ can be obtained by differentiating (9) and using the power terms of (11). Therefore, the following matrix expression is obtained:

$$\frac{d\left[v_{c_{1\alpha}^{\Sigma\Delta}} v_{c_{2\alpha}^{\Sigma\Delta}} v_{c_{0\alpha}^{\Sigma\Delta}} v_{c_{1\beta}^{\Sigma\Delta}} v_{c_{2\beta}^{\Sigma\Delta}} v_{c_{0\beta}^{\Sigma\Delta}} v_{c_{\alpha 0}^{\Sigma\Delta}} v_{c_{\beta 0}^{\Sigma\Delta}}\right]^T}{dt} \approx \frac{\left[P_{1\alpha}^{\Sigma\Delta} P_{2\alpha}^{\Sigma\Delta} P_{0\alpha}^{\Sigma\Delta} P_{1\beta}^{\Sigma\Delta} P_{2\beta}^{\Sigma\Delta} P_{0\beta}^{\Sigma\Delta} P_{\alpha 0}^{\Sigma\Delta} P_{\beta 0}^{\Sigma\Delta}\right]^T}{nC\bar{v}_c}. \tag{12}$$

Using (12), and the $\alpha\beta 0\Sigma\Delta$ powers of (11), the state-space equations for the CCVs can be obtained as

$$\dot{\boldsymbol{x}}^v \approx \boldsymbol{A}^v \boldsymbol{x}^v + \boldsymbol{B}^v \boldsymbol{u}^v + \boldsymbol{d}^v \tag{13}$$

where $\boldsymbol{A}^v$ is a 8×8 zero matrix, and matrices $\boldsymbol{B}^v$, $\boldsymbol{x}^v$, $\boldsymbol{u}^v$ are defined as

$$\boldsymbol{x^v} = \begin{bmatrix} v_{c_{1\alpha}^{\Sigma\Delta}} & v_{c_{2\alpha}^{\Sigma\Delta}} & v_{c_{0\alpha}^{\Sigma\Delta}} & v_{c_{1\beta}^{\Sigma\Delta}} & v_{c_{2\beta}^{\Sigma\Delta}} & v_{c_{0\beta}^{\Sigma\Delta}} & v_{c_{\alpha 0}^{\Sigma\Delta}} & v_{c_{\beta 0}^{\Sigma\Delta}} \end{bmatrix}^T \tag{14a}$$

$$\boldsymbol{u^v} = \begin{bmatrix} i_{1\alpha}^{\Sigma\Delta} & i_{1\beta}^{\Sigma\Delta} & i_{2\alpha}^{\Sigma\Delta} & i_{2\beta}^{\Sigma\Delta} \end{bmatrix}^T. \tag{14b}$$

Using (13), (14), and (11), it is relatively simple to complete the matrices $\boldsymbol{B^v}$ and d^v. For instance, if the power $P_{1\alpha}^{\Sigma\Delta}$ of (11)(a) is considered, then the term $\frac{1}{6}(i_{2\alpha}v_{1\alpha} - i_{1\alpha}v_{2\alpha} + i_{2\beta}v_{1\beta} - i_{1\beta}v_{2\beta})$ corresponds to the first row of $\boldsymbol{d^v}$. Moreover, if the matrix $\boldsymbol{u^v}$ is expanded to consider v_{00}, i.e. in the discrete domain $\boldsymbol{u^v_{exp}}_k = [i_{1\alpha\,k}^{\Sigma\Delta}\ i_{1\beta\,k}^{\Sigma\Delta}\ i_{2\alpha\,k}^{\Sigma\Delta}\ i_{2\beta\,k}^{\Sigma\Delta}\ v_{00k}]^T$, then the term $i_{1\alpha}^{\Sigma\Delta}v_{00}$ has to be linearized because both, the voltage v_{00} and the CCs are part of the expanded control input $\boldsymbol{u^v_{exp}}_k$.

Defining $\boldsymbol{P}^{iv} = i_{1\alpha}^{\Sigma\Delta}v_{00}$ and assuming the following small signal model:

$$\boldsymbol{P}^{iv} \approx \boldsymbol{P}_0^{iv} + \boldsymbol{\Delta P}^{iv}. \tag{15}$$

The value of $\boldsymbol{\Delta P}^{iv}$ is calculated as

$$\boldsymbol{\Delta P}^{iv} \approx \left[\frac{\partial \boldsymbol{P}^{iv}}{\partial i_{1\alpha}^{\Sigma\Delta}}\right]_0 \Delta i_{1\alpha}^{\Sigma\Delta} + \left[\frac{\partial \boldsymbol{P}^{iv}}{\partial v_{00}}\right]_0 \Delta v_{00}. \tag{16}$$

In this work, it is assumed that the quiescent point [subscript '0' in (15)–(16)] corresponds to the values obtained in the previous sampling time, i.e. $t = (k-1)T_s$. Hence, $\boldsymbol{P}_0^{iv} = v_{00k-1}i_{1\alpha\,k-1}^{\Sigma\Delta}$ and the Δ values are calculated subtracting the last two samples, e.g. $\Delta v_{00} = [v_{00k} - v_{00k-1}]$. Therefore, replacing (16) in (15) yields

$$\begin{aligned}\boldsymbol{P}_k^{iv} = i_{1\alpha\,k}^{\Sigma\Delta}v_{00k} \approx v_{00k-1}i_{1\alpha\,k}^{\Sigma\Delta} + i_{1\alpha\,k-1}^{\Sigma\Delta}v_{00k} \\ - v_{00k-1}i_{1\alpha\,k-1}^{\Sigma\Delta}.\end{aligned} \tag{17}$$

Notice that in (17) the values of v_{00k-1} and $i_{1\alpha\,k-1}^{\Sigma\Delta}$ are known. Moreover, the term $-v_{00k-1}i_{1\alpha\,k-1}^{\Sigma\Delta}$ has to be added as an extra perturbation term in $\boldsymbol{d^v}$ of (13).

Using the discrete version of (14b), but augmented by v_{00k}, the control input $\boldsymbol{u^v_{exp}}_k$ of the linearized system of (13) is

$$\boldsymbol{u^v_{exp}}_k = \begin{bmatrix} i_{1\alpha_k^{\Sigma\Delta}} & i_{1\beta\,k}^{\Sigma\Delta} & i_{2\alpha\,k}^{\Sigma\Delta} & i_{2\beta\,k}^{\Sigma\Delta} & v_{00k} \end{bmatrix}^T. \tag{18}$$

Using (17)–(18), the matrices $\boldsymbol{B}_k^v$ and $\boldsymbol{d}_k^v$ in (13) are obtained and presented in (19) shown of the bottom of this page.

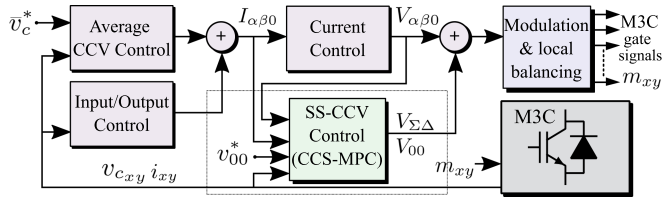

Fig. 2. Proposed CCS-MPC control strategy for the M3C.

III. Proposed CCV Control Strategy Based on Single-Stage CCS-MPC.

The proposed control system is shown in Fig. 2. As aforementioned, this article proposes a SS-CCV control based on a CCS-MPC algorithm with a single-cost function whose solution renders an optimal control action with five terms, i.e. $V_{\Sigma\Delta} = [v_{1\alpha\,k}^{\Sigma\Delta}, v_{1\beta\,k}^{\Sigma\Delta}, v_{2\alpha\,k}^{\Sigma\Delta}, v_{2\beta\,k}^{\Sigma\Delta}, v_{00k}]^T$ to simultaneously regulate

$$\boldsymbol{B}_k^{\boldsymbol{v}} = \frac{1}{nC\bar{v}_c}\begin{bmatrix} \frac{1}{3}v_{00k-1} & 0 & \frac{\sqrt{6}}{6}(v_{1\alpha k} - v_{2\alpha k}) & \frac{\sqrt{6}}{6}(v_{2\beta_k} - v_{1\beta_k}) & \frac{1}{3}i_{1\alpha\,k-1}^{\Sigma\Delta} \\ 0 & \frac{1}{3}v_{00k-1} & \frac{\sqrt{6}}{6}(v_{1\beta_k} + v_{2\beta_k}) & \frac{\sqrt{6}}{6}(v_{1\alpha k} + v_{2\alpha k}) & \frac{1}{3}i_{1\beta\,k-1}^{\Sigma\Delta} \\ \frac{\sqrt{3}}{3}v_{1\alpha k} & -\frac{\sqrt{3}}{3}v_{1\beta_k} & \frac{\sqrt{3}}{3}v_{1\alpha k} & \frac{\sqrt{3}}{3}v_{1\beta_k} & \frac{\sqrt{3}}{9}i_{2\alpha k} \\ \frac{\sqrt{6}}{6}(v_{1\alpha k} - v_{2\alpha k}) & \frac{\sqrt{6}}{6}(v_{1\beta_k} + v_{2\beta_k}) & \frac{1}{3}v_{00k-1} & 0 & \frac{1}{3}i_{2\alpha\,k-1}^{\Sigma\Delta} \\ \frac{\sqrt{6}}{6}(v_{2\beta_k} - v_{1\beta_k}) & \frac{\sqrt{6}}{6}(v_{1\alpha k} + v_{2\alpha k}) & 0 & \frac{1}{3}v_{00k-1} & \frac{1}{3}i_{2\beta\,k-1}^{\Sigma\Delta} \\ \frac{\sqrt{3}}{3}v_{1\beta_k} & \frac{\sqrt{3}}{3}v_{1\alpha k} & -\frac{\sqrt{3}}{3}v_{1\beta_k} & \frac{\sqrt{3}}{3}v_{1\alpha k} & \frac{\sqrt{3}}{9}i_{2\beta_k} \\ -\frac{\sqrt{3}}{3}v_{2\alpha k} & -\frac{\sqrt{3}}{3}v_{2\beta_k} & -\frac{\sqrt{3}}{3}v_{2\alpha k} & -\frac{\sqrt{3}}{3}v_{2\beta_k} & \frac{\sqrt{3}}{9}i_{1\alpha k} \\ -\frac{\sqrt{3}}{3}v_{2\beta_k} & \frac{\sqrt{3}}{3}v_{2\alpha k} & \frac{\sqrt{3}}{3}v_{2\beta_k} & -\frac{\sqrt{3}}{3}v_{2\alpha k} & \frac{\sqrt{3}}{9}i_{1\beta_k} \end{bmatrix} \tag{19a}$$

$$\boldsymbol{d}^v{}_k = \frac{1}{nC\bar{v}_c}\begin{bmatrix} \frac{1}{6}\left(i_{2\alpha k}v_{1\alpha k} - i_{1\alpha k}v_{2\alpha k} + i_{2\beta_k}v_{1\beta_k} - i_{1\beta_k}v_{2\beta_k}\right) + \frac{1}{3}i_{1\alpha\,k-1}^{\Sigma\Delta}v_{00k-1} \\ \frac{1}{6}\left(i_{2\beta_k}v_{1\alpha k} - i_{1\alpha k}v_{2\beta_k} - i_{2\alpha k}v_{1\beta_k} + i_{1\beta_k}v_{2\alpha k}\right) + \frac{1}{3}i_{1\beta\,k-1}^{\Sigma\Delta}v_{00k-1} \\ \frac{\sqrt{2}}{6}\left(i_{2\beta_k}v_{2\beta_k} - i_{2\alpha k}v_{2\alpha k}\right) + \frac{\sqrt{3}}{9}i_{2\alpha k}v_{00k-1} \\ \frac{1}{6}\left(i_{2\alpha k}v_{1\alpha k} - i_{1\alpha k}v_{2\alpha k} - i_{2\beta_k}v_{1\beta_k} + i_{1\beta_k}v_{2\beta_k}\right) + \frac{1}{3}i_{2\alpha\,k-1}^{\Sigma\Delta}v_{00k-1} \\ \frac{1}{6}\left(i_{2\beta_k}v_{1\alpha k} - i_{1\alpha k}v_{2\beta_k} + i_{2\alpha k}v_{1\beta_k} - i_{1\beta_k}v_{2\alpha k}\right) + \frac{1}{3}i_{2\beta\,k-1}^{\Sigma\Delta}v_{00k-1} \\ \frac{\sqrt{2}}{6}\left(i_{2\alpha k}v_{2\beta_k} + i_{2\beta_k}v_{2\alpha k}\right) + \frac{\sqrt{3}}{9}i_{2\beta_k}v_{00k-1} \\ -\frac{\sqrt{2}}{6}\left(i_{1\alpha k}v_{1\alpha k} + i_{1\beta_k}v_{1\beta_k}\right) + \frac{\sqrt{3}}{9}i_{1\alpha k}v_{00k-1} \\ -\frac{\sqrt{2}}{6}\left(i_{1\alpha k}v_{1\beta_k} + i_{1\beta_k}v_{1\alpha k}\right) + \frac{\sqrt{3}}{9}i_{1\beta_k}v_{00k-1} \end{bmatrix}. \tag{19b}$$

the CCVs and CCs. The optimization problem combines, in a single state-space formulation, the CCs and CCVs dynamics in double $\alpha\beta 0\Sigma\Delta$ frame, from (5) and (13), respectively.

A. Single-Stage Discrete-Time Model

A discrete prediction model of these variables is required to apply the CCS-MPC algorithm to control the CCV oscillations and CCs. The discrete-time model of the CC's dynamics is obtained by applying the forward Euler method to (5), with a sampling period of T_s, and is given as follows:

$$\boldsymbol{x}_{k+1}^{i} = \boldsymbol{A}_{d}^{i}\boldsymbol{x}_{k}^{i} + \boldsymbol{B}_{d}^{i}\boldsymbol{u}_{k}^{i} \tag{20}$$

where $\boldsymbol{A}_{d}^{i}$ is a 4×4 identity matrix, $\boldsymbol{B}_{d}^{i} = T_s\boldsymbol{B}^{i}$, and matrices $\boldsymbol{x}_{k}^{i}$ and $\boldsymbol{u}_{k}^{i}$ are defined as

$$\boldsymbol{x}_{k}^{i} = \begin{bmatrix} i_{1\alpha_k}^{\Sigma\Delta} & i_{1\beta\ k}^{\Sigma\Delta} & i_{2\alpha\ k}^{\Sigma\Delta} & i_{2\beta\ k}^{\Sigma\Delta} \end{bmatrix}^{T} \tag{21a}$$

$$\boldsymbol{u}_{k}^{i} = V_{\Sigma\Delta} = \begin{bmatrix} v_{1\alpha\ k}^{\Sigma\Delta} & v_{1\beta\ k}^{\Sigma\Delta} & v_{2\alpha\ k}^{\Sigma\Delta} & v_{2\beta\ k}^{\Sigma\Delta} \end{bmatrix}^{T}. \tag{21b}$$

The transformed CCVs terms from (13) are discretized using the improved Euler method [29] with a sampling period of T_s. In the discrete-time domain, the CCV dynamic model is obtained as follows:

$$\boldsymbol{x}_{k+1}^{v} \approx \boldsymbol{A}_{d}^{v}\boldsymbol{x}_{k}^{v} + \boldsymbol{B}_{d}^{v}\boldsymbol{u}_{k}^{v} + \boldsymbol{B}_{d}^{v}\boldsymbol{u}_{k+1}^{v} + \boldsymbol{d}_{d}^{v} \tag{22}$$

where $\boldsymbol{A}_{d}^{v}$ is a 8×8 identity matrix, $\boldsymbol{B}_{d}^{v} = \frac{T_s}{2}\boldsymbol{B}^{v}$, $\boldsymbol{d}_{d}^{v} = T_s\boldsymbol{d}^{v}$, and matrices $\boldsymbol{x}_{k}^{v}$ and $\boldsymbol{u}_{k}^{v}$ are defined as

$$\begin{aligned}\boldsymbol{x}_{k}^{\boldsymbol{v}} = [&v_{c_{1\alpha}^{\Sigma\Delta}\ k}\ v_{c_{2\alpha}^{\Sigma\Delta}\ k}\ v_{c_{0\alpha}^{\Sigma\Delta}\ k}\ v_{c_{1\beta}^{\Sigma\Delta}\ k}\\ &v_{c_{2\beta}^{\Sigma\Delta}\ k}\ v_{c_{0\beta}^{\Sigma\Delta}\ k}\ v_{c_{\alpha 0}^{\Sigma\Delta}\ k}\ v_{c_{\beta 0}^{\Sigma\Delta}\ k}]^{T}\end{aligned} \tag{23a}$$

$$\boldsymbol{u}_{k}^{\boldsymbol{v}} = \begin{bmatrix} i_{1\alpha\ k}^{\Sigma\Delta} & i_{1\beta\ k}^{\Sigma\Delta} & i_{2\alpha\ k}^{\Sigma\Delta} & i_{2\beta\ k}^{\Sigma\Delta} & v_{00k} \end{bmatrix}^{T} \tag{23b}$$

where u_{k}^{v} of (23b) is equal to $\boldsymbol{u}_{expk}^{v}$ in (18). For a cascade-free control, a single control input is required, i.e. $\boldsymbol{u}_{k}^{v}$ and $\boldsymbol{u}_{k}^{i}$ must be combined into one $\boldsymbol{u}_{k}$. This objective is achieved considering that the CCs are related to the voltages using (5) and (6). As aforementioned, in this work the CMV term is considered as part of the control input, and a simple solution to achieve this is to utilise the linearization procedure discussed in Section II-B [see (17)]. With this methodology the overall control input $\boldsymbol{u}_{k}$ is expanded to include v_{00k}, i.e,

$$\boldsymbol{u}_{k} = \begin{bmatrix} v_{1\alpha\ k}^{\Sigma\Delta} v_{1\beta\ k}^{\Sigma\Delta} v_{2\alpha\ k}^{\Sigma\Delta} v_{2\beta\ k}^{\Sigma\Delta} v_{00k} \end{bmatrix}^{T}. \tag{24}$$

Then, by combining the dynamics of the CCs [see (21)] and CCVs [see(22)], and modifying the state-space equations to include $\boldsymbol{u}_{k}$ of (24) yields

$$\underbrace{\begin{bmatrix}\boldsymbol{x}_{k+1}^{v}\\ \boldsymbol{x}_{k+1}^{i}\end{bmatrix}}_{\boldsymbol{x}_{k+1}} = \underbrace{\begin{bmatrix}\boldsymbol{I}_{8\times 8} & \frac{T_s}{2}\boldsymbol{B}^{v}{}_{k}\boldsymbol{O}\\ \boldsymbol{0}_{4\times 8} & \boldsymbol{I}_{4\times 4}\end{bmatrix}}_{\boldsymbol{G}}\underbrace{\begin{bmatrix}\boldsymbol{x}_{k}^{v}\\ \boldsymbol{x}_{k}^{i}\end{bmatrix}}_{\boldsymbol{x}_{k}} + \underbrace{\begin{bmatrix}\frac{T_s^2}{2}\boldsymbol{B}^{v}{}_{k}\boldsymbol{B}^{i2}{}_{k}\\ T_s\boldsymbol{B}^{i}{}_{k}\boldsymbol{O}^{T}\end{bmatrix}}_{\boldsymbol{H}}u_{k} + \underbrace{\begin{bmatrix}T_s\boldsymbol{d}^{v}{}_{k}\\ \boldsymbol{0}_{4\times 1}\end{bmatrix}}_{\boldsymbol{d}} \tag{25}$$

where $\boldsymbol{x}$ corresponds to a 12×1 vector with the eight states associated with the CCVs oscillations and four states associated with the CCs. The control action $\boldsymbol{u}_{k}$ is a 5×1 vector composed of the voltages $V_{\Sigma\Delta}$ and v_{00}; these are synthesized by the M3C to regulate the twelve states. $\boldsymbol{O}$ is a 5×4 matrix presented in the Appendix [see (A1)] and 5×5 $\boldsymbol{B}_{k}^{i2}$ is defined in (A2). Finally, the dimensions of $\boldsymbol{B}_{k}^{v}$ and $\boldsymbol{B}_{k}^{i}$ are 8×5 and 4×4, respectively.

Using (25), the state-space equation of the whole system can be written as

$$\boldsymbol{x}_{k+1} = \boldsymbol{G}\boldsymbol{x}_{k} + \boldsymbol{H}\boldsymbol{u}_{k} + \boldsymbol{d}. \tag{26}$$

A cascade-free CCS-MPC can be implemented with the methodology proposed in this section. Notice that in this work, the iterative process used to obtain the optimal control action in [27] is avoided, as well as the algorithm solving recursively more than one optimization problem discussed in [24]. Moreover, as mentioned in [7], [30], applying the improved Euler discretization method to the M3C state-space equations, ensures that the matrix $\boldsymbol{H}$ of (26) is well-conditioned and does not have rows completely filled with zeroes. As discussed in [30], this is very important to implement cascade-free control loops using CCS-MPC algorithms.

B. Cascade-Free Single-Stage CCV Control

For the single-stage CCS-MPC algorithm, the following cost function is proposed:

$$\begin{aligned}\min_{\boldsymbol{x}_{k+1},\boldsymbol{u}_{k}}\ & J = (\boldsymbol{x}_{k+1}-\boldsymbol{x}^{*})^{T}\boldsymbol{Q}(\boldsymbol{x}_{k+1}-\boldsymbol{x}^{*}) +\\ &\qquad (\boldsymbol{u}_{k}-\boldsymbol{u}^{*})^{T}\boldsymbol{R}(\boldsymbol{u}_{k}-\boldsymbol{u}^{*})\\ \text{s.t.}\quad & \boldsymbol{x}_{k+1} = \boldsymbol{G}\boldsymbol{x}_{k} + \boldsymbol{H}\boldsymbol{u}_{k} + \boldsymbol{d}\\ & -\boldsymbol{M}^{i} \le \boldsymbol{L}^{i}\boldsymbol{x}_{k+1} \le \boldsymbol{M}^{i}\\ & -\boldsymbol{M}^{v} \le \boldsymbol{L}^{v}\boldsymbol{u}_{k} \le \boldsymbol{M}^{v}.\end{aligned} \tag{27}$$

This is a typical cost function for M3C converters, similar to those discussed in [7] and [19] where the deviation of the 12 state variables with respect to their references, at the time step $k+1$, are penalized using the diagonal matrix $\boldsymbol{Q}$. The weights in the diagonal matrix $\boldsymbol{R}$ penalize the control actions, i.e. the CMV and other voltages depicted in (24) avoiding fast variations in the vector $\boldsymbol{u}_{k}$. According to [31], the matrix $\boldsymbol{R}$ is crucial in avoiding a deadbeat-like performance, which typically exhibits fast dynamic performance but poor robustness [31]. In this work, all references are set to zero to minimise circulating currents and voltage fluctuations, except for the control action related to the CMV. The reference for this control action corresponds to a third harmonic of one of the M3C ports (it is assumed that one of the ports operates as input with a fixed frequency) to regulate the fluctuations of the CCVs and, at the same time, minimising the voltage utilization of the converter [1], [4]. Notice that the matrices $\boldsymbol{Q}$ and $\boldsymbol{R}$ have to be positive definite and positive semidefinite, respectively, to ensure a convex cost function [32]. In this work, the weighting matrices are diagonal and defined as shown as follows:

$$\boldsymbol{Q} = \text{diag}\left(\lambda_{1\alpha}^{\Sigma\Delta v}, \lambda_{1\beta}^{\Sigma\Delta v}, \lambda_{0\alpha}^{\Sigma\Delta v}, \lambda_{2\alpha}^{\Sigma\Delta v}, \lambda_{2\beta}^{\Sigma\Delta v}, \lambda_{0\beta}^{\Sigma\Delta v},\right.$$

$$\lambda_{\alpha 0}^{\Sigma\Delta v}, \lambda_{\beta 0}^{\Sigma\Delta v}, \lambda_{1\alpha}^{\Sigma\Delta i}, \lambda_{1\beta}^{\Sigma\Delta i}, \lambda_{2\alpha}^{\Sigma\Delta i}, \lambda_{2\beta}^{\Sigma\Delta i}\Big)$$

$$\boldsymbol{R} = \text{diag}(\lambda_{1\alpha}^{\Sigma\Delta *}, \lambda_{1\beta}^{\Sigma\Delta *}, \lambda_{2\alpha}^{\Sigma\Delta *}, \lambda_{2\beta}^{\Sigma\Delta *}, \lambda_{00}^{*}). \tag{28}$$

The values of the weighting factors in the matrices $\boldsymbol{Q}$ and $\boldsymbol{R}$ are adjusted using the branch and bound algorithm [33]. This algorithm utilizes a binary search methodology, augmented with simulation work to estimate suitable weight values for $\boldsymbol{Q}$ and $\boldsymbol{R}$. This adjustment is performed offline and establishes the priorities for the cost function in (27), to consider a tradeoff between good regulation of the state variables and the effort required for control actions. Moreover, even when (28) considers 17 weights; they can be grouped into six different sets. For instance, all the weights penalising the fluctuations of the CCs around their references, i.e., weights $[\lambda_{1\alpha}^{\Sigma\Delta i}, \lambda_{1\beta}^{\Sigma\Delta i}, \lambda_{2\alpha}^{\Sigma\Delta i}, \lambda_{2\beta}^{\Sigma\Delta i}]$ have the same values because all the circulating currents have identical importance. The same occurs with four of the five weights in the matrix $\boldsymbol{R}$, i.e. the values of $[\lambda_{1\alpha}^{\Sigma\Delta *}, \lambda_{1\beta}^{\Sigma\Delta *}, \lambda_{2\alpha}^{\Sigma\Delta *}, \lambda_{2\beta}^{\Sigma\Delta *}]$ are identical. Other weights with mostly equal values are those penalising the capacitor voltage fluctuations in the matrix $\boldsymbol{Q}$. In summary, only six different values are required for the 17 weights used in the cost function of (27). The experimental validation section shows the performance of the proposed control strategy considering different weighting factors and its effect on the regulation of state variables and control actions.

Constraints are used to limit the CCs and voltages to some predefined maximum values. These constraints are represented by the matrices $\boldsymbol{M}$ and $\boldsymbol{L}$, while the superscript i or v indicates if it is a cluster current constraint, acting on the circulating currents, or a CCV or CMV limit constraint, acting on the control action, respectively. The cluster current and voltage limits in the cluster xy are given by $-I_{\max} \leq i_{xy} \leq I_{\max}$ and $-CCV_{xy} \leq v_{xy} \leq CCV_{xy}$. However, the strategy used in this work requires defining the constraints as a function of the transformed currents and voltages in double $\alpha\beta 0\Sigma\Delta$ coordinates. This is presented in Appendix with the current constraints being shown in (A3) and the voltage constraints in (A4). Because of the similarity in the positive/negative limits, only one of the inequations is shown in (A3)-(A4). Notice that the constraints in the CMV, i.e., $v_{00\min} \leq v_{00k} \leq v_{00\max}$ is considered by adding an additional column in (A4).

The optimization problem of (27) can be simplified by replacing the equality constraint in the cost function of (27) and also by using (20) in the CC constraints. The results obtained are shown in the reduced cost function below

$$\min_{\boldsymbol{u}_k} J = \frac{1}{2}\boldsymbol{u}_k{}^T \boldsymbol{F}\boldsymbol{u}_k + \boldsymbol{c}^T\boldsymbol{u}_{\boldsymbol{k}}$$
$$\text{s.t.} \quad -\boldsymbol{M} \leq \boldsymbol{L}\boldsymbol{u}_k \leq \boldsymbol{M} \tag{29}$$

with

$$\boldsymbol{F} = \boldsymbol{H}^T\boldsymbol{Q}\boldsymbol{H} + \boldsymbol{R} \tag{30a}$$

$$\boldsymbol{c}^T = (\boldsymbol{x}_k^T\boldsymbol{G}^T + \boldsymbol{D}^T - \boldsymbol{x}^{*T} - \boldsymbol{u}^{*T}\boldsymbol{R}^T)\boldsymbol{Q}\boldsymbol{H}. \tag{30b}$$

With this methodology, the CCs, CCVs, and CMV constraints depend on the control actions.

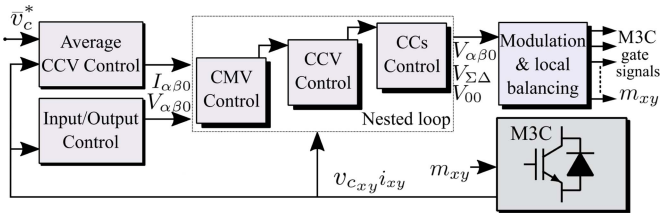

Fig. 3. CCS-MPC algorithm based on three nested control loops, which is reported in [24].

C. M3C External Control

As shown in Fig. 2, the control loops of the input/output ports, which depend on the specific converter application (e.g., machine drives, LFAC applications), together with the control of $\bar{v}_c$, the average value of the CCVs, provide the voltage references $V_{\alpha\beta 0}$ from (2) for the converter. Since the $v_{c_{00}^{\Sigma\Delta}}$ term is related to all the energy stored in the M3C capacitors and has a slow dynamic behaviour decoupled from the CCs and CMV, it is regulated by a simple PI controller acting on the power component of the port-one currents [see (10)].

The voltage references obtained by the proposed single-stage CCV control system ($V_{\Sigma\Delta}$ and V_{00}) and external-port control systems ($V_{\alpha\beta 0}$) discussed in the previous sections are transformed to the natural reference frame. After that, a LS-PWM is used to synthesise the voltage references for each power cell [34]. A sorting algorithm is utilized to balance the voltages in the floating capacitors [11], within a cluster.

IV. Comparing the Performance of the Proposed CCS-MPC With Other Control Algorithms.

In this section, the performance of the proposed CCS-MPC algorithm is compared with that of two control strategies previously reported in the literature. The first control strategy is based on a nested CCS-MPC algorithm, incorporating the state-of-the-art work of [24] in this comparison, because it also utilizes the CMV as a control input. The second control strategy is a conventional SISO control system, which was extensively discussed in [2] and is based on SISO-designed PI controllers.

The three nested CCS-MPC algorithms of [24] are depicted in Fig. 3. In this approach, the CMV is iteratively and optimally calculated by the outer controller. The computed CMV is then used as an input to the middle CCS-MPC algorithm, which calculates the reference values for the four circulating currents defined in (21a). The innermost control stage, located on the right side of Fig. 3, consists of proportional controllers that regulate the circulating currents based on the references provided by the intermediate stage. The CCS-MPC strategy proposed in [24] considers only current constraints. In contrast, the proposed CCS-MPC approach introduced in this work incorporates both voltage and current constraints for the M3C.

To ensure repeatability in the comparison, simulation work is used in this section. The PLECS software is utilized to implement the model of a 27-SM M3C and load, using the parameters

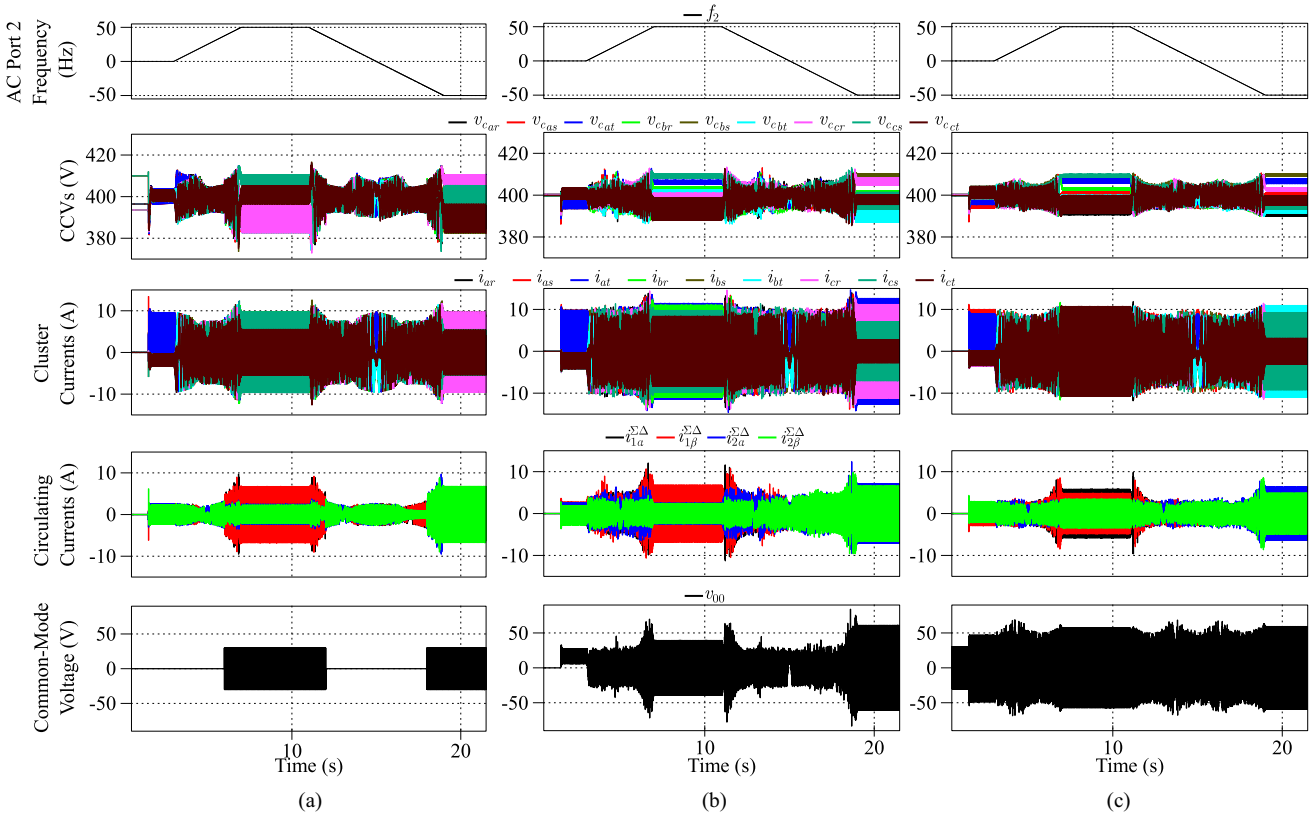

Fig. 4. Results operating over the full frequency range, including ±50 Hz operation at the output port. (a) The method based on PI controllers, which is discussed in [2]. (b) The iterative MPC method used for adjusting the CMV and CCs, discussed in [24]. (c) The proposed CCS-MPC algorithm.

TABLE I
SYSTEM PARAMETERS

Description	Variable	Value
Rated output power	P	3 kW
Number of cells		27
Cluster/ac port 1 inductances	L/Labc	2.5 mH
Module capacitance/Voltage	C/$\overline{v}_c$	2200 μF / 133.33 V
Line-to-line rms voltage	V_{abc}	220.45 V
Load parameters	R_{rst}/L_{rst}	12 Ω / 5 mH
Carrier frequency	f_s	5 kHz

shown in Table I. The system is evaluated under varying output frequencies ranging between ±50 Hz.

A. Comparing the Performance of the Proposal With Two Control Strategies

The results of the M3C operating across the full frequency range, including ±50 Hz at the output port, and considering nominal output current and a switching frequency of 5 kHz, are presented in Figs. 4 and 5. Notice that the leftmost column presents the results of [2], the middle one shows the results of [24], and the proposal performance is shown at the right column. As shown in the second row of Fig. 4, the CCVs are adequately regulated around the 400 V reference, using the three strategies considered. Nevertheless, the strategy based on [2], which utilizes PI controllers, exhibits the largest amplitude in the CCV oscillations during the test. Conversely, the proposed CCS-MPC algorithm produces the lowest amplitude of CCV oscillations. Furthermore, for the proposal, a smooth transition in the oscillations is observed throughout the test (see third row of Fig. 4), consistent with the experimental results provided in Section V-B. The CCV oscillations obtained from the method reported in [24] are also lower than those shown by [2] in the left column of Fig. 4, although not as low as those obtained with the proposed strategy. Moreover, the strategy reported in [24] produces the highest cluster currents because, in that control scheme, higher CCs are required to regulate the CCVs (see third and fourth rows of Fig. 4). In addition, it is highlighted that during the whole frequency variation test, the lowest peaks in the cluster currents are achieved with the CCS-MPC algorithm proposed in this work. Finally, the CMV used by each method throughout the test is shown at the bottom row of Fig. 4. More information about the CMV waveforms are presented in Fig. 5 and discussed below.

The simulation results obtained from the control methods when operating in steady-state with 50 Hz and 49 Hz at the input/output ports, respectively, are shown in Fig. 5. The first row of Fig. 5 shows the CCVs depicting that the lowest peak oscillations are obtained with the proposed CCS-MPC method. In addition, in the second row of Fig. 5 it is demonstrated that the cluster currents with the lowest peak amplitude are those obtained using the proposed strategy, as the algorithm minimises, through the cost function, the CCs necessary to

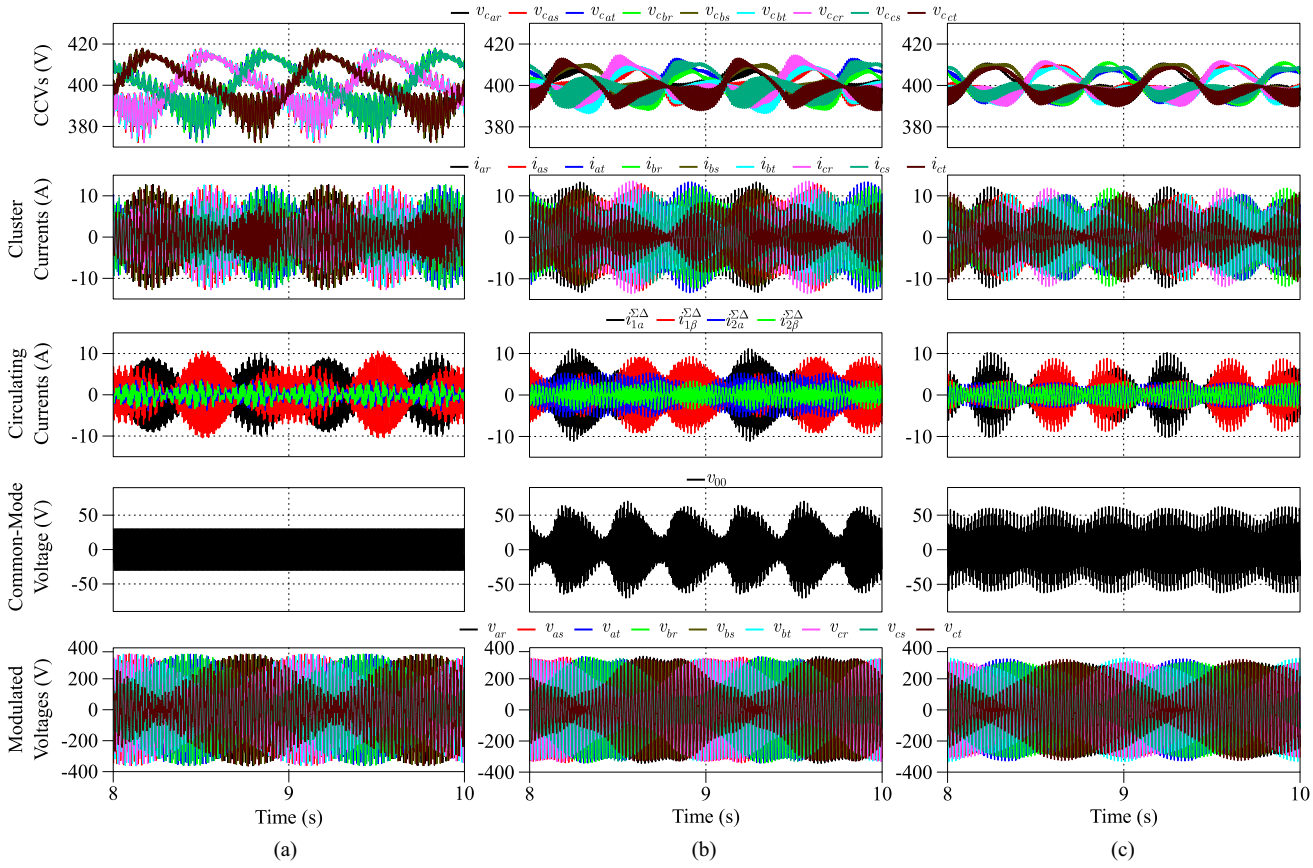

Fig. 5. Comparison of the Simulation Results Obtained in Steady-State with the Three Control Strategies $f_1 = 50$ Hz and $f_2 = 49$ Hz. a) The method based on PI controllers, as discussed in [2]. (b) The iterative MPC methodology used for adjusting the CMV and CCs, discussed in [24]. (c) The proposed CCS-MPC algorithm.

regulate the CCVs (see the CC waveforms in the third row of Fig. 5). In the fourth row, the CMVs are depicted, while the bottom row shows the total voltages to be modulated by each cluster. It should be noted that although at first glance the CMV waveforms calculated with the proposed method seems to be much higher than those obtained with the algorithm of [2] and comparable with those obtained using the algorithms reported in [24], the proposed CCS-MPC modulates total cluster voltages with the lowest amplitude. This reduction is mainly produced because the third harmonic of the input 50 Hz waveform, as well as the third harmonic of the output 49 Hz waveform, are automatically introduced by the proposed CCS-MPC algorithm into the CMV when the cost function of (27) is solved online using the active set method. Therefore, with these two CMVs, the peak amplitudes of the input and output voltages are reduced, resulting in a decrease in the total modulation depth required to operate the M3C.

For the test results corresponding to Figs. 4 and 5, a quantitative comparison of the main variables that determine the performance of the converter control is presented in Table II. The results highlight that the proposed CCS-MPC algorithm consistently outperforms the other two control methods reported in [2] and [24].

The execution time has also been measured in the compared control strategies and depicted in Table II. The execution times

TABLE II
COMPARISON OF THE PERFORMANCE OBTAINED WITH THE THREE CONTROL STRATEGIES

Variable	Method based in [2]	Method based in [24]	Proposed CCS-MPC Algorithm
ΔCCV (V)	43	28	22
$i_{xy\,RMS}$ (A)	4.41	4.38	3.86
$i_{xy\,MAX}$ (A)	12.8	13.4	12.2
CCV utilization (%)	91.75	86.25	81.25
Processing time (μs)	25	41	45

have been obtained with the ControlDesk [35] application available on the dSPACE MicroLabBox I control platform. The control algorithm based on [24] requires $\approx$41 μs, whereas the method proposed in this work takes $\approx$45 μs to run on the same platform, i.e., about 9.7% slower. However, the proposed strategy uses more constraints, as it limits the voltage to be modulated as well as the cluster currents, while the cascaded algorithm of [24] only applies constraints to the currents. In contrast, the strategy based on [2] requires $\approx$25 μs to run on the platform. The low processing burden of SISO-designed PI controllers is due to implementation simplicity [11]; however, as aforementioned, SISO controllers can hardly eliminate the cross-coupling between control loops [19].

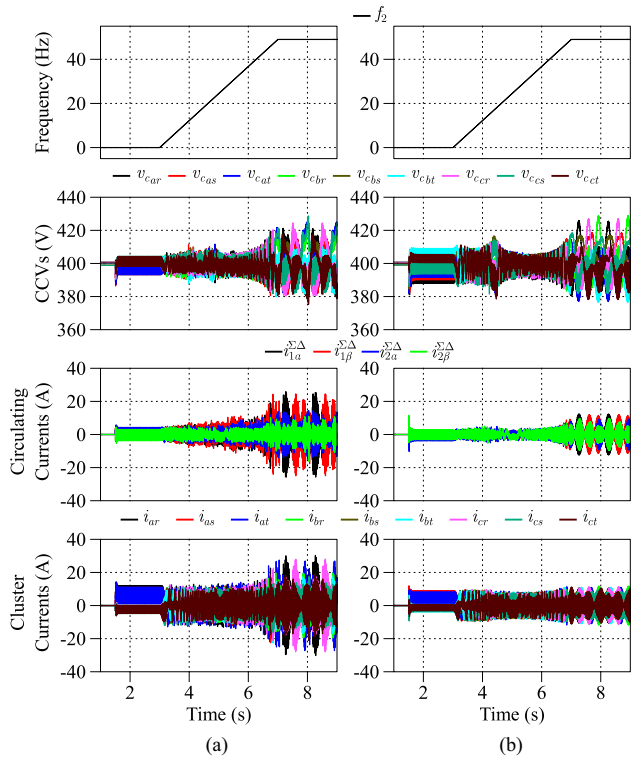

Fig. 6. Low switching frequency operation of the CCS-MPC algorithms compared in this work. (a) Results obtained with the nested CCS-MPC algorithm proposed in [24]. (b) Results obtained with the proposed CCS-MPC.

B. Low Switching Frequency Operation

As discussed in [25] and [36], cascade-free CCS-MPC algorithms offer certain advantages over nested MPC controllers when operating at low switching frequencies. To assess the dynamic response of the proposal in this operating condition, the performance of the cascade-free CCS-MPC algorithm is compared with that of [24] using a switching frequency of 500 Hz, i.e., a sampling interval of 2 ms. For a fair comparison, the weighting factors of both MPC algorithms have been tuned to yield similar peak voltage variations in the CCVs (see the second row of Fig. 6).

For the test of Fig. 6 an output frequency variation from 0 to 49 Hz is performed. The third row of Fig. 6 shows the CCs of both control methodologies. Notice the relatively large CC peaks produced by the nested CCS-MPC algorithm of [24]. This is due to the low dynamic response of the nested control loops, where a significant time delay exists between the outer CCS-MPC algorithm, where the CCs references are calculated, and the inner control loops, where these currents are regulated. Moreover, it is difficult to implement voltage constraints for the CCS-MPC discussed in [24], because the CMV is calculated in the outermost CCS-MPC, and the voltages required to impose the CCS are calculated in the inner CCS-MPC.

At the right side of Fig. 6 (third and fourth rows), the CCs and the total cluster currents are shown. Notice the significant reduction in CCs produced by the cascade-free CCS-MPC proposed in this work. This is due to: 1) the improved dynamic response achieved by a single CCS-MPC algorithm, where the CMV and the voltage required to drive the CCs are directly generated and output to the modulator in a single time step, without introducing delays, which reduce the dynamics of the control system; 2) as aforementioned, the implementation of adequate voltage constraints in the cascaded-free CCS-MPC algorithm, as well as the utilization of third-harmonic waveforms of the input and output ports in the CMV, allows a better usage of the voltage available in the capacitors. Therefore, a larger CMV could be synthesized to reduce the peak values of the CCs, without producing overmodulation.

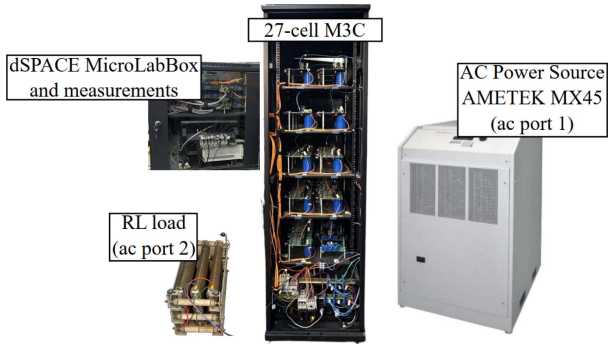

Fig. 7. M3C experimental setup.

V. Experimental Results

The proposed control strategy is experimentally validated using an M3C experimental prototype built at the Power Electronics Laboratory of the University of Chile (see Fig. 7). The M3C is implemented using 27 H-bridge modules, i.e., three full H-bridges per arm. A dSPACE MicroLabBox platform is used to control the system; this controller is composed of a Freescale QorIQ P5020 dual-core 2 GHz processor and an Xilinx Kintex-7 XC7K325 T FPGA. The FPGA performs an IPD-PWM modulation scheme and a sorting algorithm in this implementation. The carrier frequency is 5 kHz, corresponding to a 200 μs sampling time (T_s). The dSPACE processor executes the double $\alpha\beta 0\Sigma\Delta$ transforms, solves the cost function of (27) and implements the active-set solver used in this work (see [18]).

At the input port abc, a 45 kW AMETEK Programmable Power Source Model MX45 is connected to the M3C using 2.5 mH inductances, which have been selected considering lab availability. At the output port rst, an $R-L$ passive load is connected. Using some simplifications, which are discussed in [37], this load can produce similar currents and voltages at the output port of the M3C as those produced by an induction machine. Notice that the utilization of an R-L load to test the performance of control systems is used in other applications [38]. The system parameters are depicted in Table I.

A. Steady-State Performance With Different Weights on CMV

Two steady-state tests were performed by regulating the CCVs at 400 V, with an active power of 2.85 kW at the load port, at 50 Hz and 49 Hz at the input and load ports, respectively. This operating point is critical in the M3C because the input and

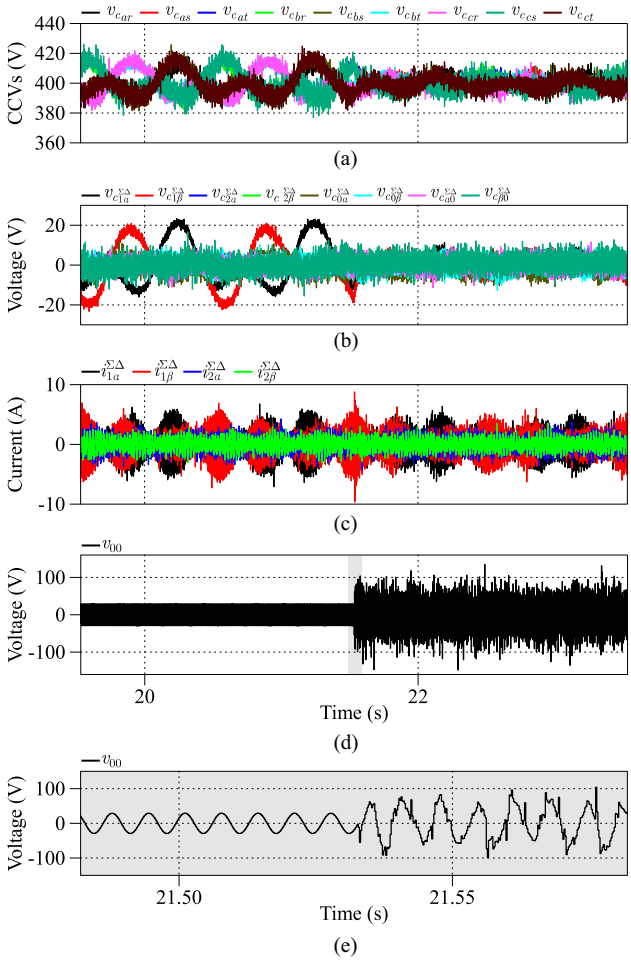

Fig. 8. Experimental results obtained with different weights on CMV. (a) 9 CCVs. (b) 8 voltage states. (c) CCs. (d) CMV. (e) Amplified view of the CMV showing the grey shaded area of (d).

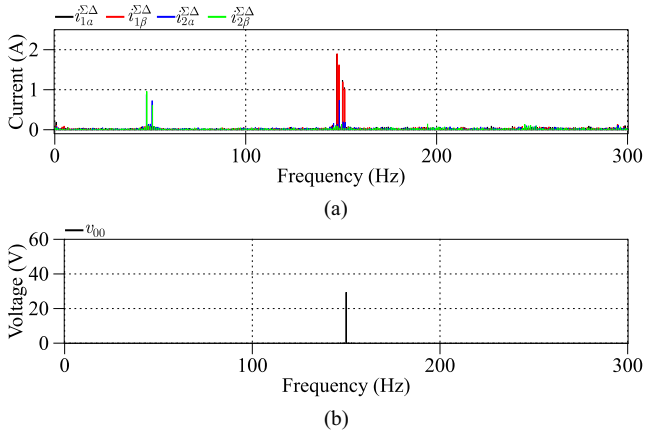

Fig. 9. Frequency spectrum with $\lambda_{00}^{*} = 0.1$. (a) CCs. (b) CMV.

output frequencies are almost equal, and the M3C operates with relatively large power.

Fig. 8 shows the experimental results that illustrate (from top to bottom) the nine CCVs, the eight voltage states, the four CCs and the CMV. At $t = 21.5$ s, the weight λ_{00}^{*} [see (28)] associated with the regulation of the CMV in the cost function is step changed from 0.1 to 0.005. These weight values are selected to obtain maximum CCV oscillations of $\approx \pm 25$ V ($\lambda_{00}^{*} = 0.1$) and $\approx \pm 10$ V for $\lambda_{00}^{*} = 0.005$. When the weight is significant, the CMV tracks with negligible error the third-harmonic reference to reduce the cost of (29). Conversely, when λ_{00}^{*} is low, then higher deviations from the reference are allowed in the CMV because the cost represented by the term $\lambda_{00}^{*} \times (v_{00} - v_{00}^{*})^2$ is much lower. This change in weighting factor, or priority, in the cost function represents a tradeoff between improving CCV regulation and increasing the control action effort, in this case, for the CMV.

Fig. 8(a) shows the correct regulation of the CCVs around the 400 V reference and the variation in the magnitude of the oscillations after the weight factor is step-changed. Fig. 8(b) shows the regulation of the voltage states around 0 V; notice that before the λ_{00}^{*} step, the states $v_{c_{1\alpha}^{\Sigma\Delta}}$ and $v_{c_{1\beta}^{\Sigma\Delta}}$, whose magnitudes are larger when $f_1 \approx f_2$, are predominant in the CCVs. After the change in λ_{00}^{*}, these states significantly reduce their oscillations, improving the CCV regulation. Fig. 8(c) shows the CCs imposed by the CCS-MPC algorithm, showing that no significant change in the circulating currents is required to obtain a better regulation of CCVs with the new weight factor. Fig. 8(d) and (e) show the change in the shape and magnitude of the CMV during this test when λ_{00}^{*} is changed from 0.1 to 0.005. An increase in the magnitude of this voltage and a change in the CMV waveform shape are observed. Moreover, fast dynamic spike-like changes are produced in the CMV to maintain good regulation when the weight is reduced.

Notice that an increase in the CMV magnitude is expected if lower CCs are produced. The balancing of the states $v_{c_{1\alpha}^{\Sigma\Delta}}$ and $v_{c_{1\beta}^{\Sigma\Delta}}$ is achieved by manipulating the powers $P_{1\alpha}^{\Sigma\Delta}$ and $P_{1\beta}^{\Sigma\Delta}$ of (11). These power variations are produced by i) the CCs interacting with the CMV and input/output voltages and ii) the CMV interacting with the CCs and input/output currents. If the CCs are reduced, the CMV could be increased to obtain a similar power variation. Note that the first row of each term of (11) depends exclusively on the AC port variables. If the M3C is operated with 50 Hz and 49 Hz at the input and load ports, respectively, the interaction between the ports' voltages and currents will generate two terms with 1 Hz power oscillations, two with 99-Hz power oscillations, two with 100-Hz oscillations and two with 98-Hz oscillations. All these power components must be compensated for using the CCs and the CMV as control actions. Therefore, the shape and magnitude of the CCs and CMV waveforms are automatically calculated when the constrained cost function of (29) is online solved.

Fig. 9(a) shows the frequency spectrum of the CCs corresponding to $\lambda_{00}^{*} = 0.1$. As aforementioned, the CCS-MPC algorithm automatically calculated the CC optimal frequency components required to regulate the CCVs; in this case, CCs frequency components of 48 Hz, 51 Hz, 148 Hz, 149 Hz, and 151 Hz are mainly obtained. These components interact with the input and output port voltages and the CMV, whose frequency

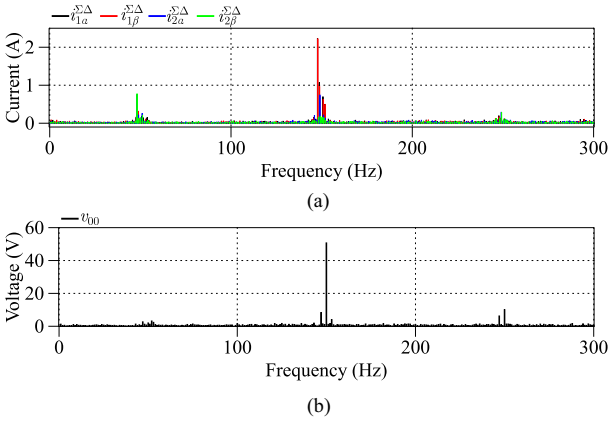

Fig. 10. Frequency spectrum with $\lambda^*_{00} = 0.005$. (a) CCs. (b) CMV.

spectrum is shown in Fig. 9(b); as expected, for $\lambda^*_{00} = 0.1$ the CMV is mainly composed of the 150 Hz and 30 V component set as a reference. The power compensating terms are explained as follows; the 48 Hz and 51 Hz CCs interact with the 49 Hz and 50 Hz port voltages, respectively, to compensate for the relatively large oscillations of 1 Hz (i.e. $f_1 - f_2$) produced in $P^{\Sigma\Delta}_{1\alpha}$, $P^{\Sigma\Delta}_{1\beta}$, $P^{\Sigma\Delta}_{2\alpha}$ and $P^{\Sigma\Delta}_{2\beta}$ of (11). While the 148 Hz and 149 Hz components of the CCs interact with the 49 Hz and 50 Hz port voltages, respectively, to compensate for the 99 Hz (i.e., $f_1 + f_2$) oscillations produced in $P^{\Sigma\Delta}_{1\alpha}$, $P^{\Sigma\Delta}_{1\beta}$, $P^{\Sigma\Delta}_{2\alpha}$, and $P^{\Sigma\Delta}_{2\beta}$ of (11). In addition, the 48 Hz and 148 Hz CCs components interact with the 50 Hz port voltages to compensate for 98 Hz (i.e., $2f_2$) oscillations produced in $P^{\Sigma\Delta}_{0\alpha}$ and $P^{\Sigma\Delta}_{0\beta}$ of (11), and the 51 Hz and 149 Hz CCs components interact with the 49 Hz port voltages to compensate for 100 Hz (i.e., $2f_1$) oscillations produced in $P^{\Sigma\Delta}_{\alpha 0}$ and $P^{\Sigma\Delta}_{\beta 0}$ of (11). Furthermore, to compensate for the dominant large oscillations of 1 Hz in $P^{\Sigma\Delta}_{1\alpha}$, $P^{\Sigma\Delta}_{1\beta}$, $P^{\Sigma\Delta}_{2\alpha}$, and $P^{\Sigma\Delta}_{2\beta}$ of (11), the 149 Hz and 151 Hz CCs components interact with the 150 Hz CMV providing additional compensating power. Notice that the CCS-MPC automatically generates all the frequency components of the CCs and CMV. They are not predefined signals as those utilized in [2] and [15].

Fig. 10(a) presents the frequency spectrum of the CCs for $\lambda^*_{00} = 0.005$, showing a decrease in the 51 Hz and 149 Hz components, from 0.7 to 0.2A and from 1.5 to 1A, respectively, when compared to the values shown in Fig. 9(a). However, there is a slight increase from 1.9 to 2.2A in the 148 Hz CC component that interacts with the CMV, whose frequency spectrum is shown in Fig. 10(b). Notice that for $\lambda^*_{00} = 0.005$, the CCS-MPC algorithm automatically injects CMV components of the third harmonic of the output port, i.e., 147 Hz, 10V. This 147 Hz component, as well as the CMV frequency components at $\approx$ 50 Hz, 150 Hz and 250 Hz, interacts with the CCs of 48 Hz and 148 Hz, and the input/output port currents. This interaction produces power terms to compensate the CCV oscillation frequency components at $2f_1$, $2f_2$, $(f_1 - f_2)$ and $(f_1 + f_2)$. Moreover, as discussed above, by reducing the weighting factor λ^*_{00}, there is an increase in the 150 Hz peak of the CMV, from 30 to 50V. Notice that with the new CMV waveform the effective value of the CCs are reduced in 7.5% respect to the value achieved for $\lambda^*_{00} = 0.1$.

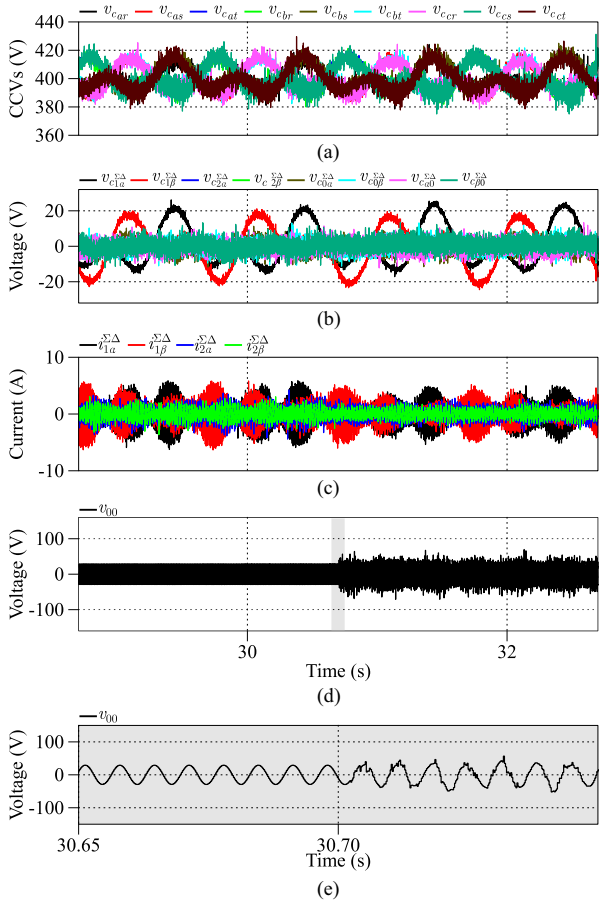

Fig. 11. Experimental results obtained with different weights on voltage states and CMV. (a) 9 CCVs. (b) 8 voltage states. (c) CCs. (d) CMV. (e) Amplified view of the CMV showing the grey shaded area of (d).

Fig. 11 shows the results of a second steady-state test, with a step-change in the value of λ^*_{00}, at $t = 30.7$ s between the same values considered in the previous experimental test. For this test, the weight factors of the voltage states are adjusted to keep the CCV oscillations in approximately the same range for the two λ^*_{00} considered. Fig. 11(a) shows that the CCVs remain regulated around 400V (natural coordinates) and a voltage variation of $\approx \pm 25$ V during the whole test. This is due to the regulation of the voltage states, as shown in Fig. 11(b), around 0V with constant amplitude oscillations. However, Fig. 11(c) shows a considerable change in the CCs, reducing their maximum and RMS values by about 20%. Again, this reduction is mainly due to the variation in the magnitude and shape of the CMV waveform, which has a relatively low increase from 20.6V RMS to 26.4V RMS when the weighting factors are changed. The CMV waveform is shown in Fig. 11(d) and (e).

The decrease in CCs is also depicted in the frequency spectrum shown in Fig. 12(a), where a reduction in the amplitude of all frequency components, with respect to those shown in Fig. 9(a), is observed. In Fig. 12(b) ($\lambda^*_{00} = 0.005$), the frequency spectrum shows that the CCS-MPC algorithm is again automatically injecting frequency components into the CMV, obtaining similar voltage fluctuation magnitudes in the CCVs, with a much smaller peak and RMS value in the CCs. After

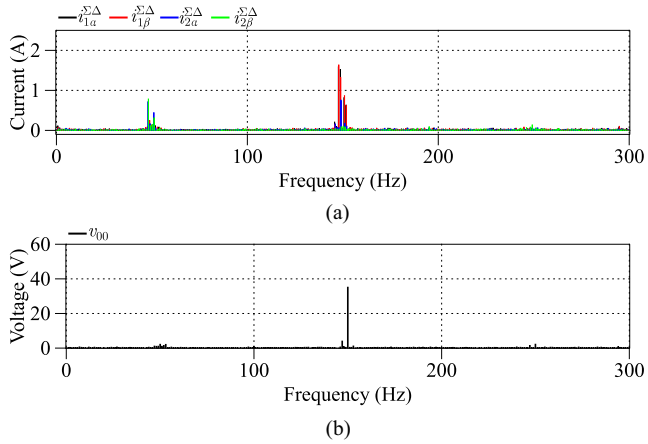

Fig. 12. Frequency spectrum with $\lambda^*_{00} = 0.005$ and 30 V variation in the CCVs. (a) CCs. (b) CMV.

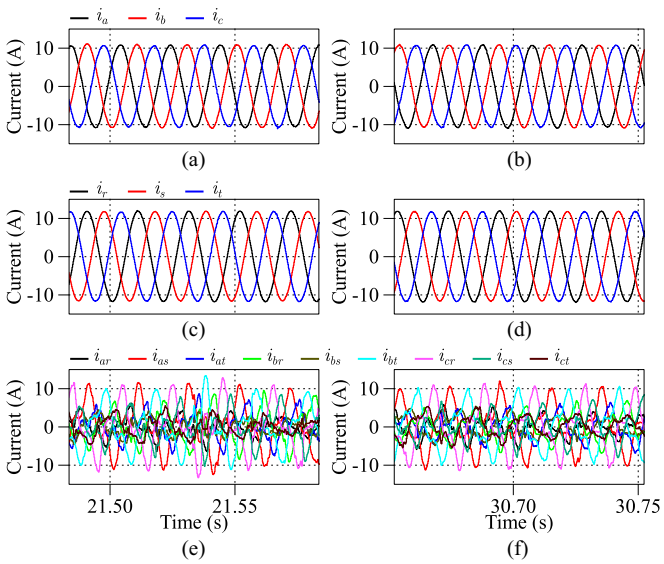

Fig. 13. Experimental results corresponding to the test shown in Fig. 8 which considers a step change in λ^*_{00} at $t = 21.5$ s (shown at the left-hand side) and experimental results corresponding to the test shown in Fig. 11 which consider a λ^*_{00} step change at $t = 30.7$ s and regulation of the CCV to a constant value (shown at the right hand-side). (a)–(b) Input port current. (c)–(d) Load port current. (e)–(f) Cluster currents.

changing the weighting factor to $\lambda^*_{00} = 0.005$, the CMV is modified and contains 7V at 147 Hz and 35V at 150 Hz, with smaller frequency components at $\approx$ 50 Hz and 250 Hz. Again, these CMV components interact with the input/output currents and the CCs to produce the compensating power terms required to regulate the CCVs.

Fig. 13 shows, from top to bottom, the currents at the input port, at the load, and at the converter clusters. These currents correspond to the experimental tests depicted in Fig. 8 (shown on the left-hand side of Fig. 13) and Fig. 11 (shown on the right-hand side of Fig. 13). Notice that the input and output currents do not show distortion with a reduced Total Harmonic Distortion (THD) of less than 3% for both experimental tests. Moreover, the step changes in λ^*_{00} neither introduce perturbations in the input currents, see Fig. 13(a) and (b) nor in the output currents, see Fig. 13(c) and (d), demonstrating that the improved control of the CCVs and reduction of currents do not affect the input and output ports. Moreover, the additional frequency components introduced by the CCS-MPC algorithm in the CCs and CMV are not reflected in any way in the input and output ports, showing the perfect decoupling achieved by the proposed control system.

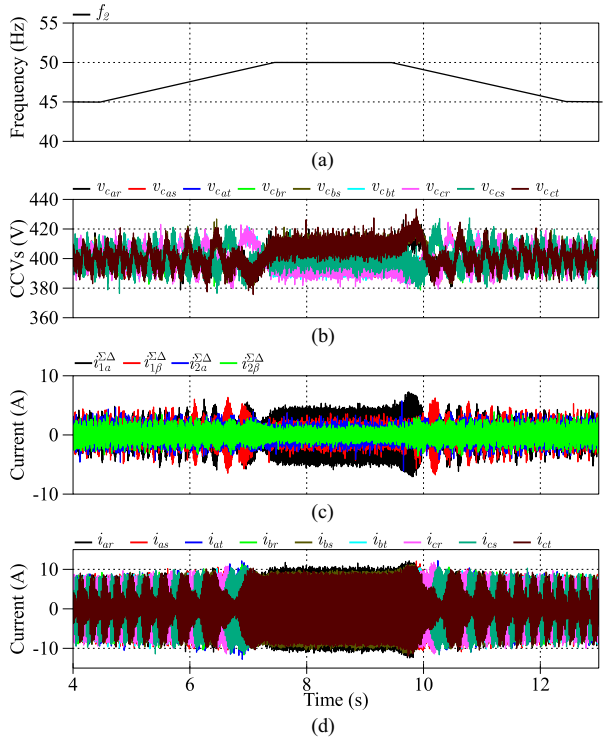

Fig. 14. Experimental results in equal frequency operation and weight on CMV $\lambda^*_{00} = 0.1$. (a) Load port frequency. (b) CCVs. (c) CCs. (d) Cluster currents.

B. Dynamic Performance

In this section, experimental tests are performed to demonstrate the effectiveness of the proposed strategy during dynamic operation. For the first test, the input side is connected to a 50 Hz power supply, and a ramp variation in the load-side frequency is performed, from 45 to 50 Hz, holding at 50 Hz for 3 s at this critical M3C operating condition [2], before returning to 45 Hz. In addition, the voltage at the load is changed proportionately to the frequency, varying the power between 2.4 kW and 3 kW, mimicking the behavior of an induction machine operating at variable frequency and high torque. This test is performed using two λ^*_{00} values to study the performance of the proposed strategy when the weight factor is reduced and the CCS-MPC algorithm automatically calculates the CMV waveform to be synthesized.

Fig. 14(a) shows the load frequency during the test. While Fig. 14(b)–(d) show the CCVs, CCs and cluster currents when using a large $\lambda^*_{00} = 0.1$ CMV weight factor. For this weight value, the CMV is mainly composed of the reference, i.e. a third harmonic of the input port. Notice the relatively large overshoot produced

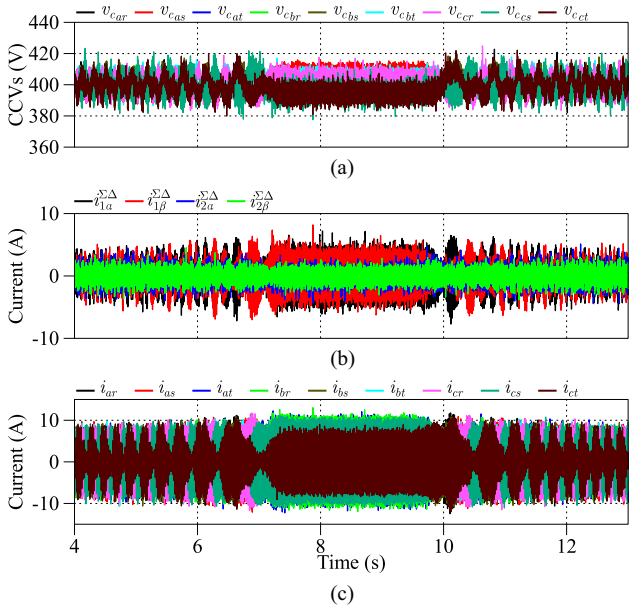

Fig. 15. Experimental results in equal frequency operation and weight on CMV $\lambda^*_{00} = 0.007$. (a) CCVs. (b) CCs. (c) Cluster currents.

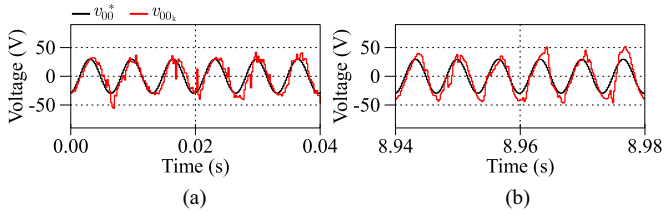

Fig. 16. Experimental results for variable frequency operation. In black is the CMV reference value, and in red is the CMV optimal value obtained from the algorithm. (a) Input output frequencies of $f_1 = 50$ Hz and $f_2 = 45$ Hz. (b) Input output frequencies of $f_1 = 50$ Hz and $f_2 = 50$ Hz, respectively.

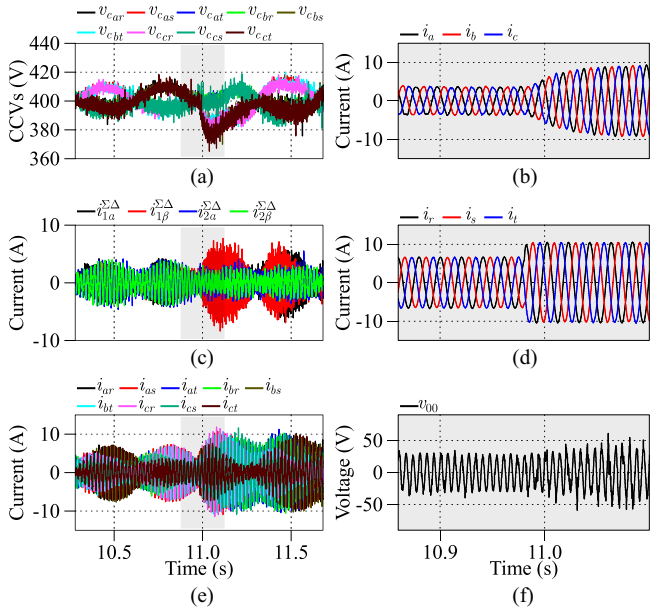

Fig. 17. Experimental results of sudden load injection. (a) 9 CCVs. (b) Input port currents. (c) CCs. (d) Output port currents. (e) Cluster currents. (f) CMV.

just before $t = 10$ s in the CCVs [Fig. 14(b)], CCs [Fig. 14(c)] and the cluster currents in Fig. 14(d).

Fig. 15(a)–(c) show the CCVs, CCs and cluster currents when the weight factor on the CMV is reduced to $\lambda^*_{00} = 0.007$. By giving the algorithm more freedom to change the shape of the CMV, the regulation of the CCVs in the equal input/output frequency operation is considerably improved. In addition, the transition in voltages and currents when operating near 50 Hz is enhanced by reducing the large peak values shown in Fig. 14. In fact, at approximately $t = 9.9$ s the CCVs reach 421V with $\lambda^*_{00} = 0.1$ and 407V with $\lambda^*_{00} = 0.007$. The smaller weight factor also has an impact on the CCs because the overshoot in the CCs is reduced from 7.2A peak to 6.4A. Notice that the proposed CCS-MPC algorithm does not require any modification to operate at equal frequencies at the input/output ports because the optimal algorithm automatically adapts itself to this critical operating condition.

The proposed CCS-MPC has also been tested considering operation at $\lambda^*_{00} = 0.007$, considering low frequency, low power, i.e. 10 Hz 0.3 kW and 0 Hz 0.1 kW, mimicking the operation of an electrical machine operated at low frequency constant torque. The regulation of the CCVs is simple to achieve using low CCs. Moreover, the deviation of the CMV from the third harmonic reference waveform is low for both frequencies. These results are in broad agreement with those reported in [39], where it is stated that the M3C is well suited to operate induction machines at low rotational speed with high torque. The CMV waveforms corresponding to operation with $\lambda^*_{00} = 0.007$ are shown in Fig. 16. Fig. 16(a)–(b) show the 150 Hz reference in black and, in red, the voltage calculated by the algorithm at 45 Hz and 50 Hz, respectively. During frequency variation, the CCS-MPC algorithm automatically calculates the additional frequency components required to maintain the CCV oscillations well-regulated. For steady-state operation at 45 Hz [see Fig. 16(a)], there are some fast variations in the CMV, but there is still a relatively good tracking of the CMV reference. For 50 Hz operation in both the input and output ports [see Fig. 16(b)], a critical operating point for the M3C [15], the tracking of the CMV reference has a relatively large error and, as expected, additional frequency components are added to the CMV which are required to maintain low CCV oscillations. This behaviour is one of the advantages of the proposed CCS-MPC algorithm; the fast dynamic of the CMV can be used to compensate fast variations in the CCVs, for instance, the overshoots shown in Fig. 14(a).

To verify the performance of the proposed CCS-MPC algorithm considering fast perturbation while operating with similar frequencies at the input/output ports, a load step, from 1 kW to 2.3 kW, is performed at the output side when the system is operating at steady state 50 Hz/49 Hz at the input/output ports respectively ($\lambda^*_{00} = 0.007$). Fig. 17(a) shows the CCVs regulated at 400V before the load step (produced at $t = 10.98$ s), with a voltage dip of about 25V after the load step at $t \approx 11.04$ s. The control system recovers the CCV in less than 0.1s to an acceptable band. Fig. 17(c) shows the CCs outputted by the

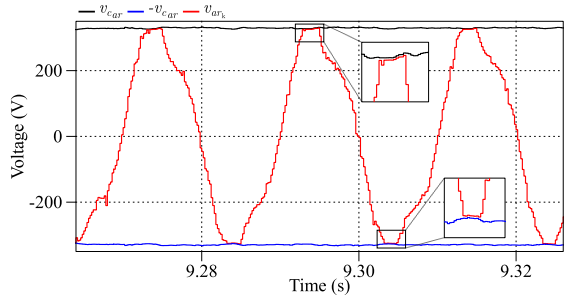

Fig. 18. Experimental results with active CCV limitation. CCV upper (black) and lower (blue) limit and reference cluster voltage (red).

CCS-MPC algorithm to regulate the CCVs at the new operating point, increasing the cluster currents as shown in Fig. 17(e). Fig. 17(b) and (d) depict the currents of the input and output ports, respectively, showing low- distortion waveforms. Furthermore, Fig. 17(f) shows the CMV outputted by the proposed linearized CCS-MPC algorithm, where a fast response to the step disturbance is performed by increasing the CMV injection to recover the CCV magnitudes immediately after the load impact and also supporting their regulation at the new operating point.

C. Performance of the Proposed Strategy Considering Constraints

To validate the operation of the voltage constraint in (29), the CCVs are regulated to 328 V instead of 400 V to force a reduction in the voltage margin available for modulation; therefore, it is easier to test the limitation of the control action experimentally. The CMV is limited to a maximum peak of 60 V, and the frequency at the output port is 49 Hz, with an active power of 2.85 kW. To evaluate only the performance of the voltage constraints, the constraints limiting the cluster currents are disabled during this test.

Fig. 18 shows the voltage modulated by a cluster and its respective limits given by the instantaneous values of the CCV. Fig. 18 shows a close-up of the maximum and minimum values available, where it is observed that the proposed constrained CCS-MPC algorithm limits the modulated voltage by adopting the CCVs oscillation waveform, taking full advantage of the available voltage and avoiding overmodulation. The effect of the constrained operation on the CCVs is shown in Fig. 19. Fig. 19(a) shows the regulation of the CCVs around the 328 V reference with fluctuations in an acceptable range throughout the test. Because of the frequency difference of 1 Hz, there is a periodic increase in the CCV oscillations observed at $t = 9.65$ s. However, the proposed CCS-MPC algorithm automatically calculates the CCs and CMV waveforms required to regulate the CCVs, as shown in Fig. 19(b)–(c). Note the fast dynamic response of the CCs to compensate for the spikes produced in the CCVs. The CMV generated by the algorithm is shown in Fig. 19(d). This voltage is mainly composed of third harmonic components from both ports, which are successfully limited at 60 V by the constraints set in (29). The CMV also has a fast dynamic response to compensate for the CCV disturbance.

The scope shot shown in Fig. 20 displays, from top to bottom, the voltage on a cluster capacitor, the voltage synthesized by a cluster, a current from the input port and a current from the

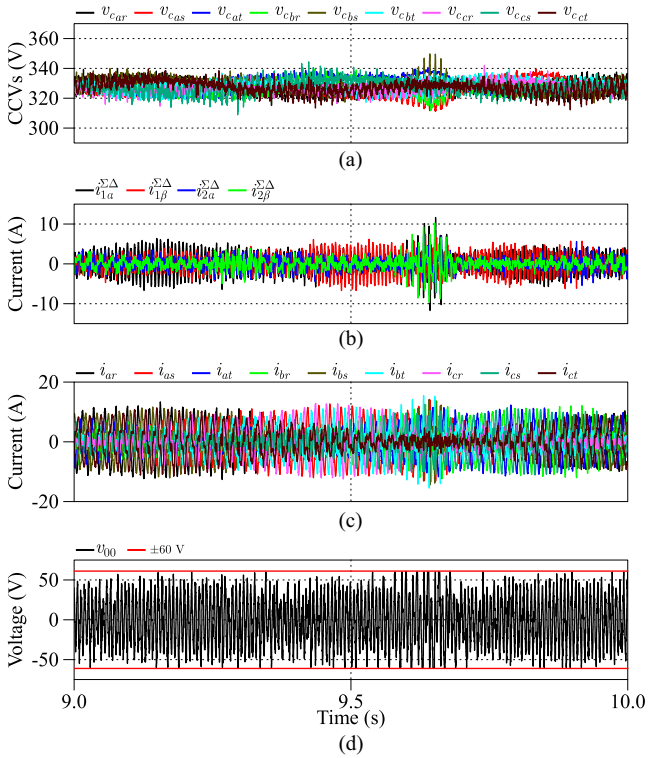

Fig. 19. Experimental results with active CCV limitation. (a) 9 CCVs. (b) CCs. (c) Cluster currents. (d) CMV.

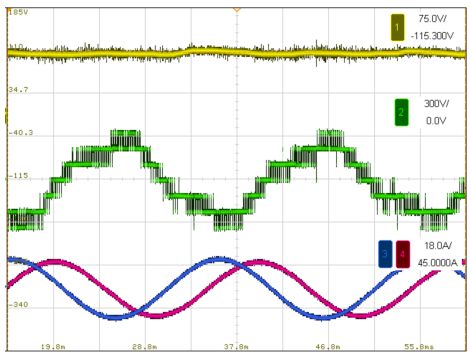

Fig. 20. Experimental results shown from top to bottom. The voltage of a capacitor in the ar cluster, the voltage synthesized by the ar cluster and currents of the a and r ports.

output port. It is observed that the capacitor voltage is correctly regulated, and the synthesized voltage is not overmodulated. Despite the slight deterioration in the control of the CCVs when the voltage constraints are active, the port currents maintain high-quality waveforms without appreciable distortion (THD less than 3%).

To demonstrate the performance of the constraints in the currents achieved by the proposed CCS-MPC algorithm, two steady-state tests are compared, considering input/output frequencies of 50 Hz and 49 Hz, respectively. For these tests, a maximum of $\pm$ 10 A has been arbitrarily selected in the cluster currents, and the voltage constraints have been disabled. The results in Fig. 21(a) and (b) show that the CCVs are correctly regulated around the 400V reference with oscillations around

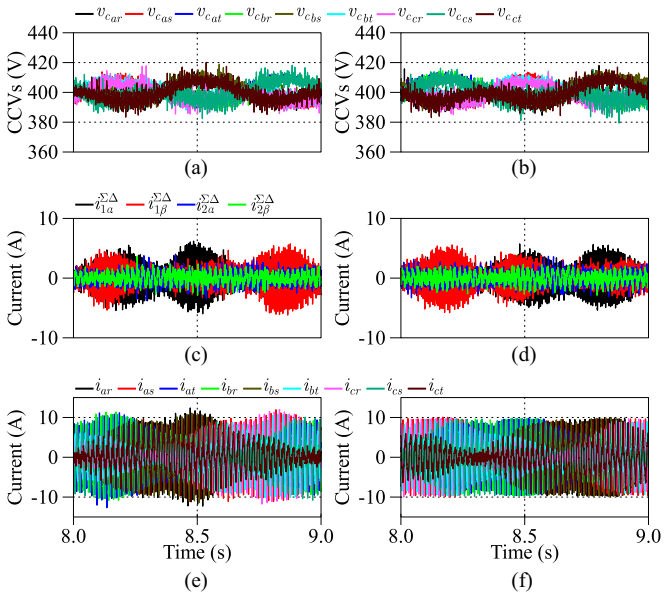

Fig. 21. Experimental results with active cluster current limitation. Left: no limitation, right: 10 A limitation. (a)–(b) 9 CCVs. (c)–(d) CCs. (e)–(f) Cluster currents.

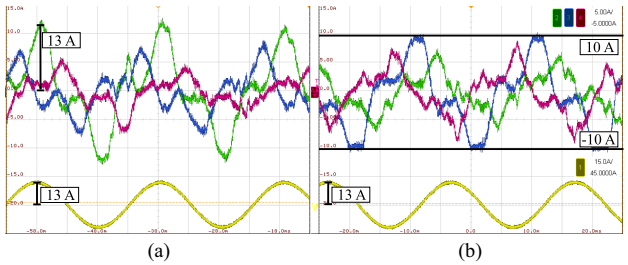

Fig. 22. Experimental results showing i_{ar}, i_{as} and i_{at} (Top), and i_a and i_r (Bottom). (a) Without enabling constraints. (b) Considering constrained operation with a $\pm$ 10 A limit for the cluster currents.

a 7.5 % band. However, with the constraints active, there is a slight increase in the fluctuations of the CCVs from 20V to 24V. Fig. 21(c) and (d) show the unconstrained/constrained CCs calculated by the proposed CCS-MPC algorithm, depicting a reduction in the peaks of the CCs shown in Fig. 21(d). The resulting cluster currents are shown in Fig. 21(e) and (f); notice the good limitation of $\pm$ 10 A achieved on all cluster currents when the constraints are activated [see Fig. 21(f).

The scope shots depicted in Fig. 22, shows the operation of the current constraints. In Fig. 22(a) is the unconstrained case, and in Fig. 22(b) is the constrained case. Each scope shot shows three cluster currents and one output port current. The results demonstrated in Fig. 22(a) depict current fluctuations well above the limits set at $\pm$ 10 A. For the constrained case, shown in Fig. 22(b), the limits are enforced by the CCS-MPC algorithm. Minor current spikes above $\pm$ 10 A occur, caused by the fact that current sampling in the control platform is not synchronized with the peak of the current ripple. However, these small overcurrents are negligible. Furthermore, it can be concluded from this experimental test that the constrained operation does not affect the quality of the input and output port currents, which maintain THD values below 3%.

VI. Conclusion

This article has introduced a cascade-free MPC strategy for the M3C, where a linearized model is applied to add the CMV as a control input. The proposed method achieves full-state regulation in a single-stage optimization process, eliminating the need for cascaded control loops or iterative procedures. Experimental results have demonstrated the advantages of this approach, highlighting the impact of CMV regulation on CCV oscillations and circulating current reduction.

The proposed control strategy effectively regulates the CCVs across a wide range of operating conditions, reducing the peak-to-peak oscillations in the CCVs with good operation at the most challenging operating point, i.e., when similar or equal electrical frequencies are present at the input/output ports of the M3C. The participation of the CCs and CMV in the regulation of the CCVs can be adjusted by modifying the respective weight factors. Suppose that a lower weight factor is applied to the CMV tracking of the third-harmonic reference. In that case, the CMV performs a more significant part in the control effort required to maintain the CCVs well-regulated, and the magnitude of the CCs could be reduced. However, when a lower weight is used, the CMV occupies more voltage margin, and a trade-off between CCs and CMV utilization could be necessary, which is relatively simple to achieve using the values of the $\boldsymbol{R}$ matrix. An additional advantage of the proposed control algorithm is that using the CMV as a control input in the linearized state-space model allows the CCS-MPC algorithm to apply constraints to both the CCs and the CMV.

Frequency-domain analysis confirms that the algorithm autonomously determines the optimal CMV components to improve CCV regulation, avoiding the need for predefined references of different frequencies and electrical sequences for both the CMV and the CCs. This methodology is typically necessary when implementing SISO control algorithms for M3C operation. According to the simulation and experimental results obtained in this research effort, under transient conditions, including CMV as a control variable may reduce the CCV deviation by more than 20%, leading to a faster recovery and improved dynamic performance.

The proposed approach has also been extensively validated under constrained operation, where the CCS-MPC algorithm regulates the converter while considering predefined voltage and current limits. Despite these constraints, the quality of the input and output currents remains unaffected, with a measured THD below 3%. The performance of the proposed method is compared with other control strategies, demonstrating its superiority in terms of CCV regulation with less control effort, reducing CCs and voltage utilization. The results confirm that integrating the CMV as an active control input in a cascade-free MPC framework enhances the performance of M3Cs, providing a new high-performance, computationally efficient control strategy alternative for high-power ac-to-ac conversion applications.

$$\underbrace{\begin{bmatrix} \frac{2}{3} & -\frac{1}{3} & -\frac{1}{3} & -\frac{1}{3} & \frac{1}{6} & \frac{1}{6} & -\frac{1}{2} & \frac{1}{6} & \frac{1}{6} \\ 0 & \frac{\sqrt{3}}{3} & -\frac{\sqrt{3}}{3} & 0 & -\frac{\sqrt{3}}{6} & \frac{\sqrt{3}}{6} & 0 & -\frac{\sqrt{3}}{6} & \frac{\sqrt{3}}{6} \\ 0 & 0 & 0 & \frac{\sqrt{3}}{3} & -\frac{\sqrt{3}}{6} & -\frac{\sqrt{3}}{6} & -\frac{\sqrt{3}}{3} & \frac{\sqrt{3}}{6} & \frac{\sqrt{3}}{6} \\ 0 & 0 & 0 & 0 & \frac{1}{2} & -\frac{1}{2} & 0 & -\frac{1}{2} & \frac{1}{2} \end{bmatrix}^T}_{\boldsymbol{L}^i} \begin{bmatrix} i_{1\alpha_k}^{\Sigma\Delta} \\ i_{1\beta_k}^{\Sigma\Delta} \\ i_{2\alpha_k}^{\Sigma\Delta} \\ i_{2\beta_k}^{\Sigma\Delta} \end{bmatrix}$$

$$\leq I_{\max} - \underbrace{\begin{bmatrix} \frac{\sqrt{2}}{3} & -\frac{\sqrt{2}}{6} & -\frac{\sqrt{2}}{6} & \frac{\sqrt{2}}{3} & -\frac{\sqrt{2}}{6} & -\frac{\sqrt{2}}{6} & \frac{\sqrt{2}}{3} & -\frac{\sqrt{2}}{6} & -\frac{\sqrt{2}}{6} \\ 0 & \frac{\sqrt{3}}{6} & -\frac{\sqrt{6}}{6} & 0 & \frac{\sqrt{6}}{6} & -\frac{\sqrt{6}}{6} & 0 & \frac{\sqrt{6}}{6} & -\frac{\sqrt{6}}{6} \\ \frac{\sqrt{2}}{3} & \frac{\sqrt{2}}{3} & \frac{\sqrt{2}}{3} & -\frac{\sqrt{2}}{6} & -\frac{\sqrt{2}}{6} & -\frac{\sqrt{2}}{6} & -\frac{\sqrt{2}}{6} & -\frac{\sqrt{2}}{6} & -\frac{\sqrt{2}}{6} \\ 0 & 0 & 0 & \frac{\sqrt{6}}{6} & \frac{\sqrt{6}}{6} & \frac{\sqrt{6}}{6} & -\frac{\sqrt{6}}{6} & -\frac{\sqrt{6}}{6} & -\frac{\sqrt{6}}{6} \end{bmatrix}^T}_{\boldsymbol{M}^i} \begin{bmatrix} i_{\alpha 0_k} \\ i_{\beta 0_k} \\ i_{0\alpha_k} \\ i_{0\beta_k} \end{bmatrix} \tag{A3}$$

$$\underbrace{\begin{bmatrix} \frac{2}{3} & -\frac{1}{3} & -\frac{1}{3} & -\frac{1}{3} & \frac{1}{6} & \frac{1}{6} & -\frac{1}{2} & \frac{1}{6} & \frac{1}{6} \\ 0 & \frac{\sqrt{3}}{3} & -\frac{\sqrt{3}}{3} & 0 & -\frac{\sqrt{3}}{6} & \frac{\sqrt{3}}{6} & 0 & -\frac{\sqrt{3}}{6} & \frac{\sqrt{3}}{6} \\ 0 & 0 & 0 & \frac{\sqrt{3}}{3} & -\frac{\sqrt{3}}{6} & -\frac{\sqrt{3}}{6} & -\frac{\sqrt{3}}{3} & \frac{\sqrt{3}}{6} & \frac{\sqrt{3}}{6} \\ 0 & 0 & 0 & 0 & \frac{1}{2} & -\frac{1}{2} & 0 & -\frac{1}{2} & \frac{1}{2} \\ \frac{1}{3} & \frac{1}{3} & \frac{1}{3} & \frac{1}{3} & \frac{1}{3} & \frac{1}{3} & \frac{1}{3} & \frac{1}{3} & \frac{1}{3} \end{bmatrix}^T}_{\boldsymbol{L}^v} \begin{bmatrix} v_{1\alpha_k}^{\Sigma\Delta} \\ v_{1\beta_k}^{\Sigma\Delta} \\ v_{2\alpha_k}^{\Sigma\Delta} \\ v_{2\beta_k}^{\Sigma\Delta} \\ v_{00_k} \end{bmatrix}$$

$$\leq \mathbf{CCV} - \underbrace{\begin{bmatrix} \frac{\sqrt{2}}{3} & -\frac{\sqrt{2}}{6} & -\frac{\sqrt{2}}{6} & \frac{\sqrt{2}}{3} & -\frac{\sqrt{2}}{6} & -\frac{\sqrt{2}}{6} & \frac{\sqrt{2}}{3} & -\frac{\sqrt{2}}{6} & -\frac{\sqrt{2}}{6} \\ 0 & \frac{\sqrt{3}}{6} & -\frac{\sqrt{6}}{6} & 0 & \frac{\sqrt{6}}{6} & -\frac{\sqrt{6}}{6} & 0 & \frac{\sqrt{6}}{6} & -\frac{\sqrt{6}}{6} \\ \frac{\sqrt{2}}{3} & \frac{\sqrt{2}}{3} & \frac{\sqrt{2}}{3} & -\frac{\sqrt{2}}{6} & -\frac{\sqrt{2}}{6} & -\frac{\sqrt{2}}{6} & -\frac{\sqrt{2}}{6} & -\frac{\sqrt{2}}{6} & -\frac{\sqrt{2}}{6} \\ 0 & 0 & 0 & \frac{\sqrt{6}}{6} & \frac{\sqrt{6}}{6} & \frac{\sqrt{6}}{6} & -\frac{\sqrt{6}}{6} & -\frac{\sqrt{6}}{6} & -\frac{\sqrt{6}}{6} \end{bmatrix}^T}_{\boldsymbol{M}^v} \begin{bmatrix} v_{\alpha 0_k} \\ v_{\beta 0_k} \\ v_{0\alpha_k} \\ v_{0\beta_k} \end{bmatrix}. \tag{A4}$$

APPENDIX

The matrices used in (25) are defined below

$$\boldsymbol{O} = \begin{bmatrix} 1 & 0 & 0 & 0 \\ 0 & 1 & 0 & 0 \\ 0 & 0 & 1 & 0 \\ 0 & 0 & 0 & 1 \\ 0 & 0 & 0 & 0 \end{bmatrix} \tag{A1}$$

$$\boldsymbol{B_k^{i2}} = \begin{bmatrix} -1/L & 0 & 0 & 0 & 0 \\ 0 & -1/L & 0 & 0 & 0 \\ 0 & 0 & -1/L & 0 & 0 \\ 0 & 0 & 0 & -1/L & 0 \\ 0 & 0 & 0 & 0 & 1 \end{bmatrix}. \tag{A2}$$

The cluster current and voltage limits are given by $-I_{\max} \leq i_{xy} \leq I_{\max}$ and $-CCV_{xy} \leq v_{xy} \leq CCV_{xy}$. The current constraints are shown in (A3) at the top of this page and the voltage constraints are shown in (A4) of the top of this page.

REFERENCES

[1] W. Kawamura, Y. Chiba, M. Hagiwara, and H. Akagi, "Experimental verification of an electrical drive fed by a modular multilevel TSBC converter when the motor frequency gets closer or equal to the supply frequency," *IEEE Trans. Ind. Appl.*, vol. 53, no. 3, pp. 2297–2306, May/Jun. 2017, doi: 10.1109/TIA.2017.2665635.

[2] M. Diaz et al., "Vector control of a modular multilevel matrix converter operating over the full output-frequency range," *IEEE Trans. Ind. Electron.*, vol. 66, no. 7, pp. 5102–5114, Jul. 2019, doi: 10.1109/TIE.2018.2870367.

[3] F. Kammerer, J. Kolb, and M. Braun, "Fully decoupled current control and energy balancing of the modular multilevel matrix converter," in *Proc. 15th Int. Power Electron. Motion Control Conf. Expo.*, IEEE, 2012, pp. 3–1, doi: 10.1109/EPEPEMC.2012.6397408.

[4] A. Christe, A. Faulstich, M. Vasiladiotis, and P. Steinmann, "World's first fully rated direct ac/ac mmc for variable-speed pumped-storage hydropower plants," *IEEE Trans. Ind. Electron.*, vol. 70, no. 7, pp. 6898–6907, Jul. 2023, doi: 10.1109/TIE.2022.3204858.

[5] M. Diaz et al., "Control of wind energy conversion systems based on the modular multilevel matrix converter," *IEEE Trans. Ind. Electron.*, vol. 64, no. 11, pp. 8799–8810, Nov. 2017, doi: 10.1109/TIE.2017.2733467.

[6] R. Himker and A. Mertens, "Operating-point-optimized control strategy for modular multilevel converters in low-frequency ac transmission systems," *IEEE Trans. Power Electron.*, vol. 39, no. 2, pp. 2334–2350, Feb. 2024, doi: 10.1109/TPEL.2023.3329373.

[7] M. Uriarte, R. Cardenas-Dobson, Y. Arias-Esquivel, M. Diaz, and O. Gomis-Bellmunt, "Continuous control set model predictive control of modular multilevel matrix converters for low-frequency AC transmission," *J. Modern Power Syst. Clean Energy*, vol. 13, no. 4, pp. 1468–1480, Jul. 2025, doi: 10.35833/MPCE.2024.000654.

[8] Y. Li, Q. Wu, Y. Jiang, J. Chen, and Q. Zhou, "Coordinated inertial response control strategy for modular multilevel matrix converter and low frequency offshore wind farm," *IEEE Trans. Ind. Appl.*, vol. 61, no. 5, pp. 7967–7976, Sep./Oct. 2025, doi: 10.1109/TIA.2025.3556796.

[9] J. Kienast, S. Bernet, and G. Sturm, "Operation, design, and losses of the modular multilevel matrix converter in a flywheel energy storage system," *IEEE Open J. Ind. Appl.*, vol. 4, pp. 336–345, 2023, doi: 10.1109/OJIA.2023.3323855.

[10] H. Akagi, "Multilevel converters: Fundamental circuits and systems," *Proc. IEEE*, vol. 105, no. 11, pp. 2048–2065, Nov. 2017, doi: 10.1109/JPROC.2017.2682105.

[11] M. Diaz et al., "An overview of modelling techniques and control strategies for modular multilevel matrix converters," *Energies*, vol. 13, no. 18, 2020, Art. no. 4678, doi: 10.3390/en13184678. [Online]. Available: https://www.mdpi.com/1996-1073/13/18/4678
[12] S. Liu, H. Zhu, X. Zhao, J. Yang, J. Nie, and Z. Shu, "Low-frequency circulating current injection in eight-component control for modular multilevel matrix converter under equal frequency," *IEEE Trans. Power Electron.*, vol. 39, no. 12, pp. 16217–16230, Dec. 2024, doi: 10.1109/TPEL.2024.3444477.
[13] J. Kienast, A. Hoffmann, M. Höer, and S. Bernet, "Novel distributed control platform and algorithm for a modular multilevel matrix converter," *IEEE Trans. Power Electron.*, vol. 38, no. 7, pp. 8089–8101, Jul. 2023, doi: 10.1109/TPEL.2023.3260241.
[14] W. Kawamura, M. Hagiwara, and H. Akagi, "Control and experiment of a modular multilevel cascade converter based on triple-star bridge cells," *IEEE Trans. Ind. Appl.*, vol. 50, no. 5, pp. 3536–3548, Sep./Oct. 2014, doi: 10.1109/TIA.2014.2311759.
[15] M. Diaz, "Control of the modular multilevel matrix converter for wind energy conversion system." Ph.D. Thesis, Dept. Elect. Eng., University of Chile, Santiago, Chile, 2017. [Online]. Available: https://repositorio.uchile.cl/handle/2250/147484
[16] F. Kammerer, J. Kolb, and M. Braun, "A novel cascaded vector control scheme for the modular multilevel matrix converter," in *Proc. Ind. Electron. Conf.*, 2011, pp. 1097–1102, doi: 10.1109/IECON.2011.6119461.
[17] S. Liu, X. Wang, Y. Meng, P. Sun, H. Luo, and B. Wang, "A decoupled control strategy of modular multilevel matrix converter for fractional frequency transmission system," *IEEE Trans. Power Del.*, vol. 32, no. 4, pp. 2111–2121, Aug. 2017, doi: 10.1109/TPWRD.2016.2646384.
[18] Y. Arias-Esquivel, R. Cardenas, L. Tarisciotti, M. Diaz, and A. Mora, "A two-step continuous-control-set MPC for modular multilevel converters operating with variable output voltage and frequency," *IEEE Trans. Power Electron.*, vol. 38, no. 10, pp. 12091–12103, Oct. 2023, doi: 10.1109/TPEL.2023.3288490.
[19] M. Urrutia, R. Cárdenas, J. C. Clare, and A. Watson, "Circulating current control for the modular multilevel matrix converter based on model predictive control," *IEEE Trans. Emerg. Sel. Topics Power Electron.*, vol. 9, no. 5, pp. 6069–6085, Oct. 2021, doi: 10.1051/e3sconf/202126101035.
[20] Y. Arias-Esquivel, R. Cardenas, M. Urrutia, M. Diaz, L. Tarisciotti, and J. C. Clare, "Continuous control set model predictive control of a modular multilevel converter for drive applications," *IEEE Trans. Ind. Electron.*, vol. 70, no. 9, pp. 8723–8733, Sep. 2023, doi: 10.1109/TIE.2022.3210515.
[21] S. Kouro, M. A. Perez, J. Rodriguez, A. M. Llor, and H. A. Young, "Model predictive control: MPC's role in the evolution of power electronics," *IEEE Ind. Electron. Mag.*, vol. 9, no. 4, pp. 8–21, Dec. 2015, doi: 10.1109/MIE.2015.2478920.
[22] R. H. Cuzmar, A. Mora, J. Pereda, P. Poblete, and R. P. Aguilera, "Long-horizon sequential FCS-MPC approaches for modular multilevel matrix converters," *IEEE Trans. Ind. Electron.*, vol. 71, no. 5, pp. 5137–5147, May 2024, doi: 10.1109/TIE.2023.3286013.
[23] M. Urrutia, R. Cardenas, J. Clare, M. Diaz, and A. Watson, "Continuous set model predictive control for energy management of modular multilevel matrix converters," *IEEE Trans. Power Electron.*, vol. 37, no. 5, pp. 5731–5748, May 2022, doi: 10.1109/TPEL.2021.3133695.
[24] B. Fan, K. Wang, P. Wheeler, C. Gu, and Y. Li, "An optimal full frequency control strategy for the modular multilevel matrix converter based on predictive control," *IEEE Trans. Power Electron.*, vol. 33, no. 8, pp. 6608–6621, Aug. 2018, doi: 10.1109/TPEL.2017.2755767.
[25] M. Preindl and S. Bolognani, "Model predictive direct speed control with finite control set of PMSM drive systems," *IEEE Trans. Power Electron.*, vol. 28, no. 2, pp. 1007–1015, Feb. 2013, doi: 10.1109/TPEL.2012.2204277.
[26] Z. Gong, L. Zhang, C. Liu, Z. Yang, and X. Wu, "Deadbeat model predictive control for modular multilevel matrix converter under unbalanced grid conditions," *IEEE Trans. Power Electron.*, vol. 40, no. 1, pp. 1258–1271, Jan. 2025, doi: 10.1109/TPEL.2024.3480357.
[27] R. H. Cuzmar, A. Mora, J. Pereda, and R. P. Aguilera, "An improved reference generator based on MPC of circulating currents and common-mode voltage for modular multilevel matrix converters," *IEEE Trans. Ind. Electron.*, vol. 72, no. 2, pp. 1958–1968, Feb. 2025, doi: 10.1109/TIE.2024.3423336.
[28] J. Gajardo, J. Pereda, R. P. Aguilera, A. Mora, R. H. Cuzmar, and P. Poblete, "Optimization-based control of modular multilevel matrix converters with integrated energy storage for simultaneous variable-speed drive and grid-feeding," *IEEE Trans. Ind. Electron.*, vol. 72, no. 8, pp. 8397–8407, Aug. 2025, doi: 10.1109/TIE.2024.3519583.
[29] A. Gilat and V. Subramaniam, *Numerical Methods for Engineers and Scientists: An Introduction With Applications Using MATLAB*, 3rd ed. Hoboken, NJ, USA: Wiley, 2013.
[30] Y. Arias-Esquivel, R. Cardenas-Dobson, M. Uriarte, M. Diaz, and L. Tarisciotti, "An advanced zero-error continuous control set model predictive controller for low voltage ride through of grid-connected power converters," *IEEE Trans. Ind. Electron.*, pp. 1–12, Aug. 13, 2025, doi: 10.1109/TIE.2025.3591703.
[31] D. E. Quevedo, R. P. Aguilera, and T. Geyer, *Predictive Control in Power Electronics and Drives: Basic Concepts, Theory, and Methods*. Cham, Switzerland: Springer International Publishing, 2014, pp. 181–226.
[32] J. Nocedal and S. Wright, "Numerical Optimization," *Springer Ser. Operations Res. and Financial Eng.*, Ed. Berlin, Germany: Springer Nature, 2006.
[33] P. Cortes et al., "Guidelines for weighting factors design in model predictive control of power converters and drives," in *Proc. 2009 IEEE Int. Conf. Ind. Technol.*, Churchill, VIC, Australia, 2009, pp. 1–7, doi: 10.1109/ICIT.2009.4939742.
[34] B. Wu and M. Narimani, *High-Power Converters and AC Drives*. Hoboken, NJ, USA: Wiley, 2017, pp. 119–141.
[35] Dspace, "ControlDesk basic training." Accessed: Aug. 2025. [Online]. Available: https://www.dspace.com/de/gmb/home/support/suptrain/controldesk/cdesk.cfm
[36] E. Fuentes, D. Kalise, J. Rodríguez, and R. M. Kennel, "Cascade-free predictive speed control for electrical drives," *IEEE Trans. Ind. Electron.*, vol. 61, no. 5, pp. 2176–2184, May 2014, doi: 10.1109/TIE.2013.2272280.
[37] F. del Blanco, M. Degner, and R. Lorenz, "Dynamic analysis of current regulators for ac motors using complex vectors," *IEEE Trans. Ind. Appl.*, vol. 35, no. 6, pp. 1424–1432, Nov./Dec. 1999, doi: 10.1109/28.806058.
[38] P. Zhao et al., "An online neural network approximator-based model-free predictive control approach for power converters," *IEEE Trans. Power Electron.*, vol. 40, no. 10, pp. 15757–15767, Oct. 2025, doi: 10.1109/TPEL.2025.3576762.
[39] Y. Okazaki et al., "Experimental comparisons between modular multilevel DSCC inverters and TSBC converters for medium-voltage motor drives," *IEEE Trans. Power Electron.*, vol. 32, no. 3, pp. 1805–1817, Mar. 2017, doi: 10.1109/TPEL.2016.2562103.

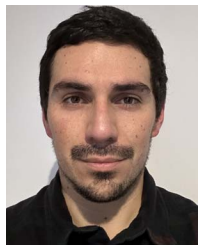

Matias Uriarte (Graduate Student Member, IEEE) received the B.Sc. and M.Sc. degrees in electrical engineering from the University of Santiago of Chile, Santiago, Chile, in 2018. He is currently working toward the Ph.D. degree in electrical engineering with the Universityof Chile, Santiago, and the Technical University of Catalonia, Barcelona Spain. His research interests include renewable energy integration in power systems and the control of modular multilevel converters.

Roberto Cardenas-Dobson (Senior Member, IEEE) was born in Punta Arenas, Chile. He received the B.S. degree in electrical engineering from the University of Magallanes, Punta Arenas, Chile, in 1988, and the M.Sc. and Ph.D. degrees in electrical and electronic engineering from the University of Nottingham, Nottingham, U.K. (PEMC group), in 1992 and 1996, respectively. He is currently a Full Professor of power electronics and drives with the Department of Electrical Engineering, the University of Chile, Santiago, Chile.Dr. Cárdenas-Dobson was the recipient of the "Ramon Salas Edwards" Prize from the Chilean Institute of Engineers in 2009. He was also awarded the 2019 Third Prize Paper Award of the IAS Industrial Power Converter Committee. He also received IEEE TRANSACTIONS ON INDUSTRIAL ELECTRONICS Best Paper Awards in 2005 and 2019. From 2014 to 2021, he was an Associate Editor for IEEE TRANSACTIONS ON INDUSTRIAL ELECTRONICS.

Yeiner Arias-Esquivel (Member, IEEE) was born in Guápiles, Costa Rica. He received the B.Sc. degree in electronic engineering and the M.Sc. degree in embedded systems from the Costa Rica Institute of Technology, Cartago, Costa Rica, in 2014 and 2016, respectively, and the Ph.D. degree in electrical engineering from the University of Chile, Santiago, Chile, in 2023.Since 2014, he has been with the Costa Rica Institute of Technology, where he currently serves as an Associate Professor. His research interests include control of modular multilevel converters, model predictive control, vibration analysis, and embedded systems.

Luca Tarisciotti (Senior Member, IEEE) received the master's degree in electronic engineering from The University of Rome "Tor Vergata", Italy, in 2009, and the Ph.D. degree in electrical and electronic engineering from the PEMC group, University of Nottingham, Nottingham, U.K., in 2015.

In 2015, he became a Research Fellow with the University of Nottingham, until 2018 when he started working as Professor with the University of Chile, Santiago, Chile. Since 2019, he has been working as an Associate Professor with the University Andrés Bello, Santiago.

Matías Díaz (Senior Member, IEEE) was born in Santiago, Chile. He received the B.Sc. and M.Sc. degrees in electrical engineering from the University of Santiago of Chile, Chile, in 2011, and the dual Ph.D. degree in electrical and electronic engineering from the University of Nottingham, U.K., and the University of Chile, Santiago, in 2017. He is currently an Associate Professor with the Department of Electrical Engineering, University of Santiago, Chile. His main research interests include power electronics, renewable energy technologies, and electromobility.

Oriol Gomis-Bellmunt (Fellow, IEEE) received the degree in industrial engineering from the School of Industrial Engineering of Barcelona, Technical University of Catalonia (UPC), Barcelona, Spain, in 2001, and the Ph.D. degree in electrical engineering from the UPC in 2007.Since 2004, he has been with the Department of Electrical Engineering, UPC, where he is currently a Professor and participates with the CITCEA-UPC Research Group. Since 2020, he has been an ICREA Academia Researcher. In 2022, he co-founded eROOTS, which is a spin-off company of CITCEA-UPC, focused on the analysis of modern power systems. His research interests include the fields linked with electrical machines, power electronics, and renewable energy integration in power systems.